

# All known Type Ia supernovae models fail to reproduce the observed bolometric luminosity-width correlation

Amir Sharon<sup>1</sup>★ and Doron Kushnir<sup>1</sup>

<sup>1</sup>*Dept. of Particle Phys. & Astrophys., Weizmann Institute of Science, Rehovot 76100, Israel*

Accepted XXX. Received YYY; in original form ZZZ

## ABSTRACT

Type Ia supernovae (SNe Ia) are widely believed to arise from thermonuclear explosions of white dwarfs (WDs). However, ongoing debate surrounds their progenitor systems and the mechanisms triggering these explosions. Recently, Sharon & Kushnir showed that existing models do not reproduce the observed positive correlation between the  $\gamma$ -ray escape time,  $t_0$ , and the synthesized  $^{56}\text{Ni}$  mass,  $M_{\text{Ni}56}$ . Their analysis, while avoiding complex radiation transfer (RT) calculations, did not account for the viewing-angle dependence of the derived  $t_0$  and  $M_{\text{Ni}56}$  in multi-dimensional (multi-D) models during pre-nebular phases, where most observations performed. Here, we aim to identify an observational width–luminosity relation, similar to the  $t_0$ – $M_{\text{Ni}56}$  relation to constrain multi-D models during pre-nebular phases while minimizing RT calculation uncertainties. We show that the bolometric luminosity at  $t \leq 30$  days since explosion can be accurately computed without non-thermal ionization considerations, which are computationally expensive and uncertain. We find that the ratio of the bolometric luminosity at 30 days since explosion to the peak luminosity,  $L_{30}/L_p$ , correlates strongly with  $t_0$ . Using a sample of well-observed SNe Ia, we show that this parameter tightly correlates with the peak luminosity,  $L_p$ . We compare the observed  $L_{30}/L_p$ – $L_p$  distribution with models from the literature, including non-spherical models consisting of head-on WD collisions and off-centered ignitions of sub-Chandrasekhar mass WDs. We find that all known SNe Ia models fail to reproduce the observed bolometric luminosity-width correlation.

**Key words:** methods: data analysis – supernovae: general.

## 1 INTRODUCTION

Type Ia supernovae (SNe Ia) are widely accepted to be the result of thermonuclear explosions of white dwarfs (WDs), but their progenitor systems and explosion mechanism remain under debate (for a review, see, e.g., Maoz et al. 2014). Several theoretical scenarios for the progenitor systems have been suggested, including a Chandrasekhar mass (Chandra) or sub-Chandrasekhar mass (sub-Chandra) WD that ignites due to some external interaction and direct WD collisions.

Predictions from these models have demonstrated agreement with certain observational characteristics of SNe Ia in specific instances. One particular set of characteristics frequently employed for model-observation comparisons is the Phillips relation (Phillips 1993; Phillips et al. 1999), which relates the maximum flux with the width of the light curve in a specific wavelength band. This relation holds significance in cosmology, and its parameters are relatively straightforward to derive from observations, rendering it a widely adopted method for such comparisons (Kasen 2006; Sim et al. 2010; Blondin et al. 2017; Shen et al. 2021a; Collins et al. 2022). However, deriving these parameters from theoretical models and simulations is quite challenging. One of the key challenges in the calculation of these parameters and of most observable quantities is radiative-transfer (RT) calculations, which often prohibit a robust compar-

ison to observations (see reviews, e.g. Hillebrandt & Niemeyer 2000; Noebauer & Sim 2019).

While advances in computational capabilities and theoretical understanding have significantly improved RT simulations, the large number of physical processes involved, particularly opacity from thousands of atomic transitions with both absorptive and scattering characteristics, prohibit comprehensive 3D calculations based on first principles. Various physical approximations — in particular, different treatments of the significant deviations from local thermodynamic equilibrium (LTE) — are employed by different RT codes to calculate the properties of the plasma and the radiation field. Additionally, approximate treatment of atomic physics is required due to the partially calibrated atomic data.

Recently, Blondin et al. (2022) compared various radiative transfer (RT) codes applied to identical benchmark models (the StaNdaRT public electronic repository<sup>1</sup>). Among the codes considered, only CMFGEN (Hillier & Miller 1998; Dessart & Hillier 2010) performs full non-local thermodynamic equilibrium (NLTE) calculations from the onset of the explosion. The properties obtained from CMFGEN, such as light curves, temperature, and ionization profiles, behave differently than those from LTE codes after a few tens of days post-explosion, highlighting the importance of NLTE treatment during

★ E-mail: amir.sharon@weizmann.ac.il

<sup>1</sup> <https://github.com/sn-rad-trans>

these phases. However, CMFGEN is computationally expensive and thus limited to 1D profiles.

One approach to bypass the radiative transfer (RT) calculation challenges is determining the  $\gamma$ -ray escape time,  $t_0$ , defined by (Jeffery 1999)

$$f_{\text{dep}}(t) = \frac{t_0^2}{t^2}, \quad f_{\text{dep}} \ll 1, \quad (1)$$

where  $t$  is the time since explosion and  $f_{\text{dep}}$  is the  $\gamma$ -ray deposition fraction, representing the portion of the generated  $\gamma$ -ray energy that is deposited in the ejecta. This quantity can be estimated directly from the ejecta or using simple  $\gamma$ -ray radiation transfer simulations (Stritzinger et al. 2006; Scalzo et al. 2014; Wygoda et al. 2019a; Guttman et al. 2024). To measure  $t_0$  in observations of SNe, the ejecta must be sufficiently optically thin so that the bolometric luminosity,  $L(t)$ , equals the instantaneous deposited energy from radioactive decay:

$$L(t) = Q_{\text{dep}}(t). \quad (2)$$

For SNe Ia, this condition is typically met at  $t \gtrsim 60$  days post-explosion for most SNe (Wygoda et al. 2019a; Sharon & Kushnir 2020b). The  $\gamma$ -ray escape time and the synthesized  $^{56}\text{Ni}$  mass have recently been used to compare models with observations for various types of SNe (Sharon & Kushnir 2020b,a, 2023). In Sharon & Kushnir (2020a), the  $t_0$ - $M_{\text{Ni}56}$  distribution of SNe Ia was compared with model predictions from the literature. It was found that none of the models reproduced the observed relation, which showed a strong, positive correlation between the two parameters. This positive correlation, similar to the Phillips relation, implies that bright SNe are characterized by slowly evolving light curves and vice versa. Additionally, there is some scatter in the observed  $t_0$ - $M_{\text{Ni}56}$  relation, which could be attributed to multi-dimensional (multi-D) effects from non-spherical explosions.

In multi-D models, the luminosity can be unevenly distributed across different viewing angles, even when the total luminosity, integrated over all angles, satisfies Equation (2). This uneven distribution might cause the inferred  $t_0$  and  $M_{\text{Ni}56}$  values to vary between viewing angles, deviating from their true values. Only at very late times ( $t \gtrsim 150$  day for typical SNe Ia), when the ejecta is in the deep nebular phase and sufficiently optically thin, does the emitted radiation become completely isotropic regardless of the ejecta's structure. However, obtaining the bolometric luminosity at these late times is quite challenging because the supernova has significantly faded, and a large portion of the flux shifts to the near- and mid-infrared wavelengths. Only a few supernovae have the required temporal and wavelength coverage, such as the recent SN 2021aefx, having JWST observations at  $t > 200$  days post-explosion (Kwok et al. 2023; Chen et al. 2023). Considering multi-D effects could explain the observed variability in the  $t_0$ - $M_{\text{Ni}56}$  distribution, allowing for more stringent constraints on non-spherical models. However, radiative transfer (RT) calculations are necessary for this purpose, and, as previously mentioned, these calculations contain significant uncertainties.

One might argue that to address RT uncertainties and calculate  $t_0$  for multi-D models, it is possible to extract the escape time from the calculated bolometric light curve by solely using times when Equation (2) holds. This method was applied to 1D ejecta in Kushnir et al. (2020), and the resulting  $t_0$  values were consistent with those obtained directly from the ejecta or through  $\gamma$ -ray RT simulations. However, a multi-dimensional structure within the ejecta complicates the use of this method to mitigate inaccuracies in bolometric light curve calculations performed by RT codes. The challenge arises because, although Equation (2) might hold for the angle-averaged luminosity

at certain times, the distribution of luminosity among different observed angles remains unknown and cannot be verified by the  $\gamma$ -ray deposition. Therefore, the luminosity of a non-spherical ejecta at a given observed angle cannot be determined free of the uncertainties associated with RT.

In this paper, we seek an observational "width-luminosity" relation, similar to the  $t_0$ - $M_{\text{Ni}56}$  relation, that would allow to constrain multi-D models at pre-nebular phases while minimizing the inherent uncertainties of RT calculations. We derive a relation that accomplishes this by imposing two constraints on the observational data. The first is that only the bolometric light curve is considered instead of observing specific bands. The second constraint is that the analysis is limited to early times,  $t < 30$  days since the explosion. We discuss the motivation for these constraints in Section 3.

Previous studies have examined the early-time bolometric properties of SNe Ia and explosion models (Contardo et al. 2000; Stritzinger et al. 2006; Phillips et al. 2006; Scalzo et al. 2014, 2019; Wygoda et al. 2019a; Gronow et al. 2021; Shen et al. 2021b). Notably, the decline in bolometric magnitude during the first 15 days after the peak,  $\Delta M_{\text{bol}}(15)$ , was found to correlate well with the  $\gamma$ -ray escape time (Stritzinger et al. 2006) and the peak luminosity,  $L_p$  (Scalzo et al. 2019), although this relation was not as tight as in individual bands (i.e., the Phillips relation). The bolometric magnitude decline rate was also used in Shen et al. (2021b) and Gronow et al. (2021) to compare simulations of non-spherical sub-Chandra explosions with SNe Ia observations from Scalzo et al. (2019). Their models broadly agreed with observations but failed to reproduce the bright segment of the observed relations, and the variations due to viewing angle were more pronounced than observed.

In this study, we utilize the early-time bolometric light curve to establish a new "width-luminosity" relation with several novel features: (1) We select the luminosity ratio 30 days post-explosion to the peak luminosity,  $L_{30}/L_p$ , as our shape parameter. This parameter, which is independent of the supernova's brightness and distance, offers better model-constraining power and corresponds to earlier times when RT simulation results are more reliable, compared to the commonly used  $\Delta M_{\text{bol}}(15)$ ; (2) We analyze several different SNe Ia explosion models from the literature, including 1D models of Chandra and sub-Chandra explosions and non-spherical 2D models of head-on collisions and off-centered sub-Chandra ignitions; (3) We utilize a high-quality sample of well-observed SNe Ia from Sharon & Kushnir (2020b) and supplement it with additional objects. By focusing on early-time observables, we require less stringent observational requirements than those needed for determining  $t_0$  and  $M_{\text{Ni}56}$ , necessitating continuous observations for at least  $\approx 100$  days post-explosion. As a result, early-time observables can be measured for a larger fraction of supernovae, significantly increasing the sample size.

We find a tight relation between the  $L_{30}/L_p$ - $L_p$  of our sample, shown as black symbols in Figure 1. This relationship exhibits a monotonic increase over the entire luminosity range, resembling the  $t_0$ - $M_{\text{Ni}56}$  correlation shown in Figure 2. Upon comparing these findings to models from the literature, we observe that none of the models reproduce the observed  $L_{30}/L_p$ - $L_p$  relation, paralleling the results found in Sharon & Kushnir (2020a).

The paper is organized as follows: In Section 2, we describe our observational data, the sample of SNe Ia, and the explosion models we have incorporated. Section 3 outlines our motivation for using the early bolometric light curve to constrain models. The resulting  $L_{30}/L_p$ - $L_p$  relation is presented in Section 4 and illustrated in Figure 1. In Section 5, we examine the opacity of the 1D models to account for the short rise times of the low-luminosity models. Our

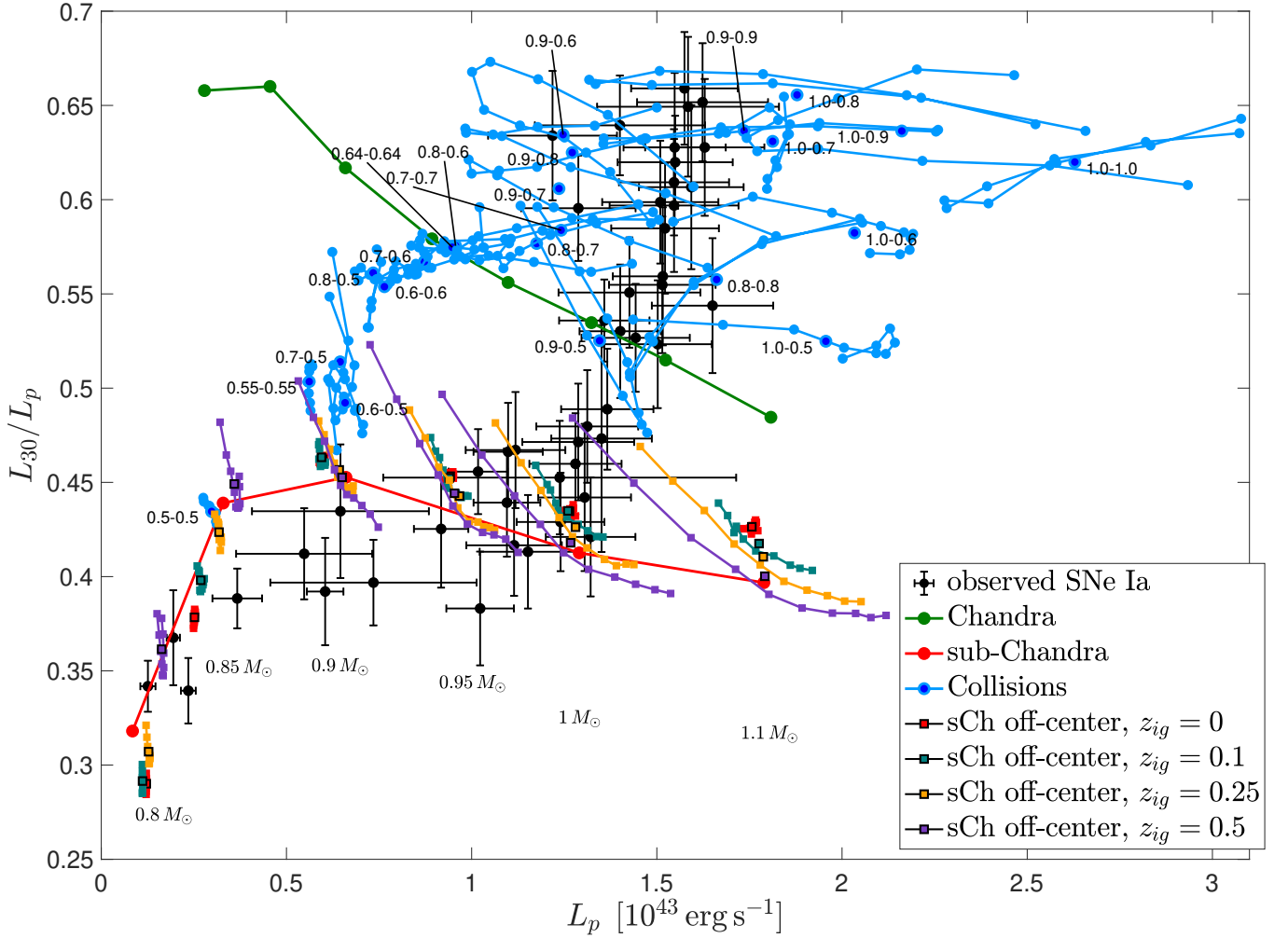


**Figure 1.** The  $L_{30}/L_p-L_p$  distribution of SNe Ia, along with 1D and 2D explosion models. Observed SNe, depicted as black circles, form a tight relation, wherein  $L_{30}/L_p$  increases monotonically with  $L_p$  throughout the entire luminosity range. 1D models consist of the Chandra explosion of Dessart et al. (2014, green line) and the sub-Chandra detonations of Kushnir et al. (2020, red line). The 2D models include direct WD collisions (Kushnir et al. 2013) and off-centered sub-Chandra ignitions (Schinasi-Lemberg & Kushnir 2024). For these models, shown are the results for different lines of sight, uniformly distributed in  $\cos \theta$ , and their angle-averaged values are indicated by a larger symbol with the same shape and a similar color, and, for the off-centered sub-Chandra models, a black-colored edge. The masses of each collision configuration are denoted in solar masses alongside their respective angle-averaged values or connected by lines. The off-centered detonations are marked according to the ignition location parameter, with red, teal, orange, and purple squares, indicating  $z_{ig} = 0, 0.1, 0.25, 0.5$ , respectively. The progenitor masses are displayed below their angle-averaged values. The  $z_{ig} = 0$  results slightly deviate from their 1D counterparts due to 2D instabilities in the thermonuclear detonation wave (see Schinasi-Lemberg & Kushnir 2024, for a detailed discussion). None of the models can account for the observed  $L_{30}/L_p-L_p$  distribution. A version of this figure in magnitude space is provided in Appendix C.

findings are discussed and summarized in Section 6. Appendix A estimates when the ionization levels of SNe Ia ejecta depart from LTE. Appendix B compares the rise time of our models to a simplified analytical solution (Kushnir & Katz 2019) to evaluate the effects of the ejecta opacity. In Appendix C, we provide some of our results in magnitude space for completeness. Tables containing the parameters of both the observed sample and the models are provided in Appendix D.

## 2 OBSERVED DATA AND MODELS

### 2.1 Observations

The observational data comprises the SNe Ia sample from Sharon & Kushnir (2020b) and Sharon & Kushnir (2023), with some

modifications<sup>2</sup>, augmented with SNe lacking late-time observations required for measuring  $t_0$  and  $M_{\text{Ni}56}$ , yet possessing sufficient early-time data for this analysis. These additional SNe, sourced from the Carnegie Supernova Project (Contreras et al. 2010; Stritzinger et al. 2011; Krisciunas et al. 2017; Burns et al. 2018), expand the sample size to 47 SNe. The photometry, distance, extinction values, and explosion time are taken from the literature. All SNe in the sample have near-infrared (NIR) photometry, contributing  $\approx 20 - 40\%$  of the total flux at times considered in this analysis (Scalzo et al. 2014; Sharon & Kushnir 2023). Bolometric light curves are constructed

<sup>2</sup> Several SNe were excluded upon reevaluation due to incomplete light curve coverage at peak, and the distance to SN 2011fe was updated using the latest Cepheid-based distance from Riess et al. (2022).

using the methods described by Sharon & Kushnir (2020b), and are available in the online supplementary material.

Following the approach of Sharon & Kushnir (2020a), we construct the  $t_0$ - $M_{\text{Ni}56}$  distribution of the sample (only for objects with adequate observations) using the methods of Sharon & Kushnir (2020b). The results, shown in Figure 2 as black symbols, align closely with the distribution in Sharon & Kushnir (2020a), as most of the samples overlap. This comparison is instructive for contrasting the bolometric width–luminosity relation (Figure 1).

Utilizing the sample of bolometric light curves, the analysis parameters for each SN are calculated as follows. The peak luminosity and time are determined by fitting a low-order polynomial to all luminosity measurements  $\{L_i\}_{i=1}^N$  with  $L_i > 0.85 \cdot \max(L_i)$ . The uncertainty in peak luminosity includes statistical errors and several systematic terms, such as uncertainties in distance, extinction, and missing UV flux (missing flux from longer wavelengths is negligible due to the required NIR coverage), all of which are propagated to the peak luminosity error. The value of  $L_{30}$  is obtained by linear interpolation. The error in the  $L_{30}/L_p$  parameter (see Section 3) is unaffected by distance uncertainty and only minimally influenced by uncertainties in extinction and missing UV flux. However, the error includes a contribution from the unknown explosion time, estimated by assuming the explosion time uncertainty is 5% of the time to the first measurement,  $\Delta t_{\text{exp}} = 0.05(t_1 - t_{\text{exp}})$ , where  $t_1$  and  $t_{\text{exp}}$  are the times of the first luminosity measurement and the estimated explosion time, respectively.

The derived parameters for the SNe sample are presented in Table D1.

## 2.2 Models

The models ejecta analyzed in this work include 1D and 2D models from the literature. The 1D models encompass explosions of Chandra WDs (Dessart et al. 2014), as well as centrally ignited sub-Chandrasekhar CO WDs with masses ranging from 0.8 to 1.1  $M_{\odot}$  (Kushnir et al. 2020). The 2D models include head-on WD collisions (Kushnir et al. 2013) and off-centered ignited sub-Chandra CO WDs (Schinasi-Lemberg & Kushnir 2024). These 2D models are axisymmetric, with their luminosity depending on the observed inclination angle  $\theta$ , measured relative to the symmetry axis ( $\theta = 0, 180^\circ$  along the symmetry axis). The off-centered ignited sub-Chandra models have the same mass range as the 1D models and include a parameter  $z_{\text{ig}} = 0, 0.1, 0.2, 0.5$ , representing the ignition position along the symmetry axis normalized by the WD radius ( $z_{\text{ig}} = 0$  corresponds to central ignition).

In all models, the explosion was simulated until the ejecta reached a state of free streaming, resulting in a homologously expanding profile. At this stage, the models'  $\gamma$ -ray escape time,  $t_0$ , can be computed through simple  $\gamma$ -ray transfer simulations or direct analytical calculations (Wygod a et al. 2019a). For consistency with Sharon & Kushnir (2020a), we present the results using the analytical calculation in this work, noting that the differences compared to simulations are within a few percent. The  $t_0$  results and the synthesized  $^{56}\text{Ni}$  mass from the explosion are provided in Table D2 and displayed in Figure 2, replicating the findings of Sharon & Kushnir (2020a); Schinasi-Lemberg & Kushnir (2024). Note that the low-luminosity sub-Chandra  $z_{\text{ig}} = 0$  ignitions show slight deviations from their 1D counterparts due to 2D instabilities in the thermonuclear detonation wave (see Schinasi-Lemberg & Kushnir 2024, for a detailed discussion). The conclusion that none of the models accurately reproduce the observed distribution remains unchanged.

To determine the models' bolometric width–luminosity relation,

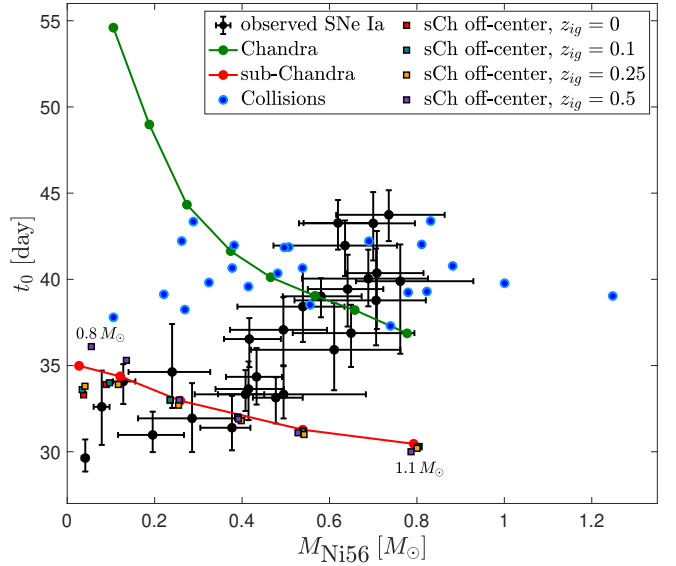


**Figure 2.** The distribution of the  $^{56}\text{Ni}$  mass,  $M_{\text{Ni}56}$ , and the  $\gamma$ -ray escape time,  $t_0$ , for the observed sample and explosion models. The symbols are the same as in Figure 1. The lowest and highest sub-Chandra progenitor mass is displayed near their respective values. Our results replicate the findings of Sharon & Kushnir (2020a); Schinasi-Lemberg & Kushnir (2024). Note that the low-luminosity sub-Chandra  $z_{\text{ig}} = 0$  ignitions show slight deviations from their 1D counterparts due to 2D instabilities in the thermonuclear detonation wave (see Schinasi-Lemberg & Kushnir 2024, for a detailed discussion). The conclusion that none of the models accurately reproduce the observed distribution remains unchanged.

we conducted RT simulations with the provided ejecta profiles to compute their bolometric light curves. These simulations were performed using the URILIGHT code (Wygod a et al. 2019a,b), a Monte Carlo code based on the approximations used in the SEDONA program (Kasen et al. 2006). The key assumptions include homologous expansion, an LTE configuration for the ions' ionization state and energy level occupation, and expansion opacities with optical depths calculated using the Sobolev approximation. The thermalization parameter  $\epsilon$ , which defines the probability that a photon absorbed in a given transition is re-emitted in a different transition, was set to 0.8.

## 3 THE BOLOMETRIC LIGHT CURVE SHAPE PARAMETER

This section presents the rationale for selecting the  $L_{30}/L_p$  shape parameter as an observable that can robustly constrain models. In Section 3.1, we identify the observed quantities RT simulations can produce with minimal uncertainty, limiting our analysis to these results. Next, we identify observables within these constraints to compare models and observations effectively (Section 3.2).

### 3.1 Identifying Minimally Uncertain Observed Quantities

The first constraint we impose is limiting the analysis to the bolometric light curve rather than comparing specific bands. The reason is that the simulated flux of a specific band is significantly more sensitive to uncertainties in the opacities of bound-bound transitions. These uncertainties can arise from incomplete atomic data, the opacity calculation method, and the material's ionization state. The

re-emission of absorbed photons redistributes the flux to other wavelengths, typically from the UV to the IR, making the total flux less susceptible to these uncertainties (Gronow et al. 2021; Shen et al. 2021a). To illustrate this claim, we use the StaNdaRT public electronic repository, focusing on the toy06 benchmark model, a  $1 M_{\odot}$  model with characteristic Ia SNe  $^{56}\text{Ni}$  mass ( $0.6 M_{\odot}$ ) and kinetic energy ( $E_{\text{kin}} = 10^{51}$  erg) values, and analytic density and composition profiles.

In Figure 3, we compare the multi-band light curves (in flux space) of the toy06 model from various RT codes<sup>3</sup> against the results of the URILIGHT code. In most bands, differences are tens of percent at most times and can exceed 50 percent. Apart from the STELLA code, variations are less pronounced in the V band but can still reach  $\approx 25$  percent. Generally, codes that show over-luminous light curves in one band tend to have under-luminous light curves in another band due to flux redistribution. Figure 4 illustrates the same comparison for the bolometric luminosity. As shown in the figure, the deviations in bolometric luminosity are smaller than in individual bands and, apart from the initial  $\approx 10$  days, are mostly within  $\approx 15$  percent.

Another effect observable in Figure 3 is that starting from  $\approx 30$  days post-explosion, the deviations significantly increase in certain bands. Additionally, the light curves of CMFGEN, the only NLTE code used during non-nebular times, deviate noticeably from the other codes. We, therefore, attribute this increased deviation at later times to the impact of NLTE effects, which become more pronounced as the density decreases. The deviation from LTE is driven by ionization and excitation caused by the thermalization of high-energy (up to a few MeV) non-thermal leptons produced in the  $^{56}\text{Ni}$  decay chain, either as decay products or as electrons up-scattered by  $\gamma$ -rays from the decay (Axelrod 1980; Kozma & Fransson 1992; Baron et al. 1996). This deviation significantly affects the material’s opacity and the SNe light curves. Non-thermal ionization is known to be the dominant ionization process in the nebular phase and, as we demonstrate below, is also significant at earlier times.

To evaluate the significance of NLTE ionization, we again utilize the StaNdaRT repository to compare the evolution of ionization structures between URILIGHT (LTE) and CMFGEN (NLTE). Figure 5 shows the results for the toy06 model, focusing on the fractional ionization levels of Co and Fe averaged across the entire ejecta. Up to  $\approx 30$  days post-explosion, the ionization levels from both codes are in good agreement. However, after this period, the ionization levels begin to diverge, with the CMFGEN ejecta becoming significantly more ionized. This divergence marks the onset of significant ionization from non-thermal leptons. Note that the abundance of Co V is lower compared to Fe V in the CMFGEN simulation. This discrepancy arises because non-thermal ionization is not included for Co IV due to a lack of atomic data<sup>4</sup>. This limitation further demonstrates the uncertainties inherent in these calculations.

In Appendix A, we use simple analytical considerations to determine when non-thermal ionization becomes significant. Our calculations show that this epoch is around 30 days post-explosion, consistent with previous findings. Consequently, we limit our analysis to the early bolometric light curve,  $t \leq 30$  days from the explosion, corresponding to times when the LTE assumption holds. Our approach aligns with the findings of Shen et al. (2021a), who compared light

curves of sub-Chandrasekhar explosions using both LTE and NLTE RT codes. They observed that 15 days past peak light, significant discrepancies arise between the two methods in the observed magnitudes across most bands, while differences at peak light are much smaller. Moreover, the bolometric luminosities were roughly similar during the considered times, up to approximately 30 days since peak light. They also examined the effect of the absorption parameter,  $\epsilon$ , in LTE simulations and found that altering its value had minimal impact on the bolometric light curve, though individual magnitudes varied starting from 15 days after peak light.

### 3.2 Selecting Observables for Model Comparison

We aim to construct a width–luminosity relation under the constraints from above, similar to the Phillips relation and the  $t_0$ – $M_{\text{Ni}56}$  distribution. The luminosity parameter we choose is, naturally, the peak bolometric luminosity. In Figure 6 we compare  $L_p$  with the late-time luminosity parameter,  $M_{\text{Ni}56}$ . Consistent with previous works (e.g., Scalzo et al. 2019), these parameters for the observed SNe Ia, shown as black symbols, display an almost perfect correlation, with a Pearson correlation coefficient of  $\rho = 0.984$ .

The selection of the shape parameter is less trivial and we choose the luminosity ratio 30 days after the explosion to the peak luminosity,  $L_{30}/L_p$ . In Figure 7, we compare  $L_{30}/L_p$  with the late-time shape parameter,  $t_0$ . Here, the correlation of the observed sample is also prominent but to a lesser extent, with a Pearson correlation coefficient of  $\rho = 0.872$ . We also fit a linear regression model between the two parameters, represented by  $L_{30}/L_p = a \cdot t_0 + b$ . The results, shown by a dashed red line, have a slope of  $a \approx 0.022 \text{ day}^{-1}$ . This approach aims to compare the ability to constrain models with the  $L_{p+15}/L_p$  parameter (see below). Given the strong correlations evident in Figures 6 and 7, we expect the positive correlation observed in the  $t_0$ – $M_{\text{Ni}56}$  relation to hold for the bolometric width–luminosity relation as well.

Figures 6 and 7 also present the same comparisons for the explosion models. For non-spherical models, the  $L_p$  and  $L_{30}/L_p$  results are shown for different values of the inclination angle  $\theta$ , evenly distributed in  $\cos \theta$ , along with their angle-averaged values. A strong correlation is evident within the models’  $M_{\text{Ni}56}$ – $L_p$  distribution, and they align with the observed relation (Figure 6). However, the behavior of the shape parameters in Figure 7 is more complex. While the models generally follow the observed relation, the collision and Chandra models represent the slowly evolving SNe Ia, whereas the sub-Chandra models only cover the quickly evolving region (this is also evident in Figure 2). Notably, the  $t_0$ – $L_{30}/L_p$  relation of the sub-Chandra models is non-monotonic. This occurs because low-mass WD progenitors exhibit short rise times (from explosion to peak light) despite having longer  $\gamma$ -ray escape times than higher-mass progenitors. We discuss this behavior further in Section 5. a  $1 M_{\odot}$  model with characteristic Ia SNe  $^{56}\text{Ni}$  mass ( $0.6 M_{\odot}$ ) and kinetic energy ( $E_{\text{kin}} = 10^{51}$  erg) Finally, we compare the  $L_p$ – $L_{30}/L_p$  relation of the models and RT codes in the StaNdaRT repository. Figure 8 displays the observed SNe Ia relation along with the RT code results for the four benchmark ejecta models in the StaNdaRT repository. These models include, in addition to the toy06 model described above, the toy01 model, which is identical to the toy06 model except for a lower  $^{56}\text{Ni}$  yield of  $0.1 M_{\odot}$ . They also include two models from the Chandra WD explosions of Dessart et al. (2014), the ddc10 and ddc25 models, with  $^{56}\text{Ni}$  yields of  $0.12$  and  $0.52 M_{\odot}$ , respectively (note that not all of the RT results are available for all models). We calculate the scatter in the  $L_{30}/L_p$  parameter for each explosion

<sup>3</sup> The RT codes are: ARTIS (Shingles et al. 2020), CMFGEN (Hillier & Miller 1998), CRAB (Utrobin 2004), KEPLER (Woosley et al. 2002), SEDONA (Kasen et al. 2006), STELLA (Blinnikov & Bartunov 1993), SUMO (Jerkstrand 2011), and SuperNu (Wollaeger et al. 2013).

<sup>4</sup> John Hillier, private communication.

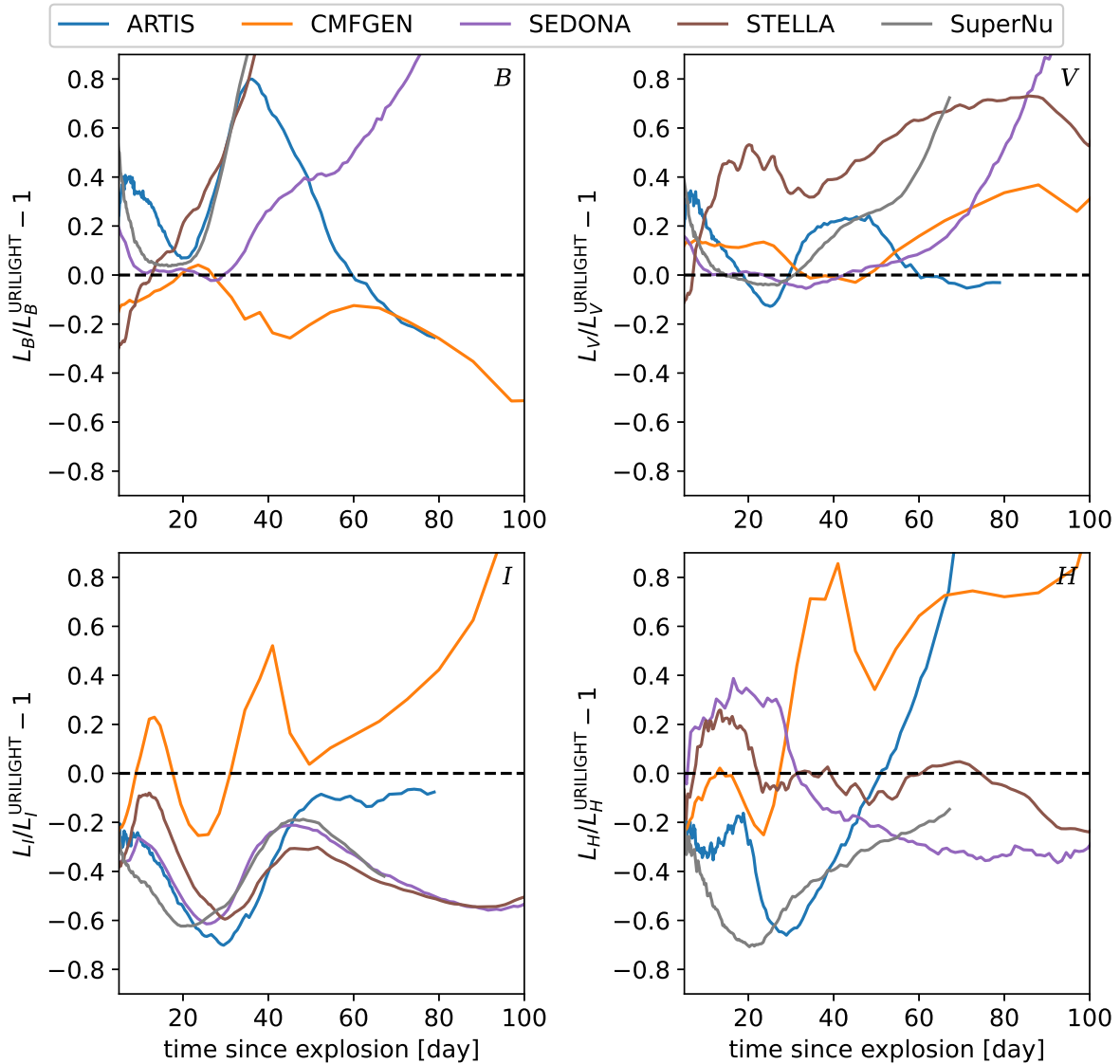


**Figure 3.** Comparison of multi-band light curves generated by various RT codes with respect to the URILIGHT code, performed on the toy06 model from Blondin et al. (2022). All data are taken from the StaNdaRT public electronic repository. Plotted is the code’s deviation from URILIGHT, in flux space, for the  $B$ ,  $V$ ,  $I$ , and  $H$  bands. All bands except the  $V$  band show deviations of tens of percents. The  $V$  band light curves are in better match, with deviations of up to 25 percent for all the codes except STELLA. After 30 days, deviations in the  $B$  and  $H$  bands substantially increase.

model among the RT codes, excluding the ARTIS results due to their significant deviation from the others. The scatter for the ‘normal’ luminosity models, toy06 and ddc10, is  $\approx 9$  and  $\approx 6$  percent, respectively. For the low-luminosity models, toy01 and ddc25, the scatter is  $\approx 15$  and  $\approx 6$  percent, respectively. The small scatter in  $L_{30}/L_P$  between models supports our choice for the shape parameter.

We also explore replacing  $L_{30}$  with the luminosity 15 days post-peak,  $L_{p+15}$ , similar to the bolometric magnitude decline rate,  $\Delta M_{\text{bol}}(15) = -2.5 \log(L_{p+15}/L_P)$ , used in previous studies (Stritzinger et al. 2006; Scalzo et al. 2019; Shen et al. 2021b). In Stritzinger et al. (2006), for a sample of 16 SNe Ia, this parameter was found to correlate well with  $t_0$ . In Scalzo et al. (2019), it was shown to correlate with  $M_{\text{Ni}56}$  and  $L_P$ . Figure 9 presents the  $L_{p+15}/L_P - t_0$  distribution of our sample. We use  $L_{p+15}/L_P$  instead of the more commonly used form of  $\Delta M_{\text{bol}}(15)$  to facilitate better comparison with the  $L_{30}/L_P$  results. The  $\Delta M_{\text{bol}}(15) - t_0$  distribution is shown in

Appendix C. Similar to Figure 7, the observed sample (black symbols) exhibits a strong correlation between these parameters, and the models show similar qualitative behavior in both relations. As with the  $L_{30}/L_P - t_0$  relation, we fit a linear regression model between these parameters and find a slope of  $\approx 0.011 \text{ day}^{-1}$ , about half of the value when using  $L_{30}/L_P$ . This result demonstrates the advantage of the  $L_{30}/L_P$  parameter in distinguishing SNe, as it changes more rapidly with respect to  $t_0$  and spans a broader range of values than the  $L_{p+15}/L_P$  parameter.

Explosion models are also better separated in Figure 7 compared to Figure 9. In the latter, high-luminosity sub-Chandra and collision models have similar  $L_{p+15}/L_P$  values despite the notable differences in their  $t_0$  values. Another drawback of using  $L_{p+15}$  is that the peak time of SNe Ia can slightly exceed 15 days, causing  $L_{p+15}$  to correspond to times later than 30 days post-explosion when NLTE effects become significant (Figure 5). Nonetheless, calculating  $L_{p+15}$

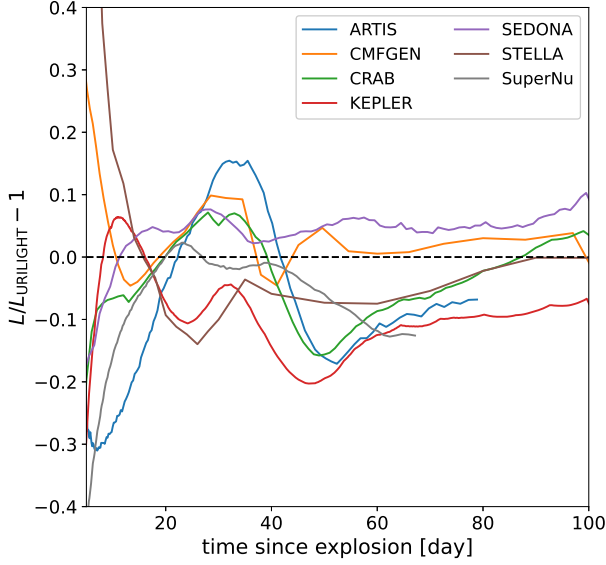


**Figure 4.** Same as Figure 3 but for the bolometric luminosity, and the comparison is against a larger set of models. Deviations here are smaller than individual bands an, apart from the initial  $\approx 10$  days, are mostly within  $\approx 15$  percent.

does not require explosion time, reducing the associated uncertainty compared to  $L_{30}/L_p$ . For completeness and to facilitate comparison with previous works, we also include  $L_{p+15}/L_p$  in our analysis.

#### 4 THE $L_{30}/L_p$ - $L_p$ DISTRIBUTION

This section compares the  $L_{30}/L_p$ - $L_p$  distribution of observed SNe Ia to various explosion models. The results are given in Appendix D and shown in Figure 1. A version of Figure 1 in magnitude space is provided in Appendix C.

Similar to the Phillips relation (Phillips 1993; Phillips et al. 1999) and to the  $t_0$ - $M_{\text{Ni}56}$  distribution (Figure 2), the observed bolometric width-luminosity relation shows a strong correlation between the shape and luminosity of SNe Ia, where bright SNe are slower and vice versa. Our results are broadly consistent with Figure 10 of Scalzo et al. (2019), where this trend is also noticeable. However, our sample covers a wider range of luminosities, and our relation using the  $L_{30}/L_p$  parameter exhibits greater precision, within  $\approx 10$  percent in either the luminosity or  $L_{30}/L_p$ , compared to their relation using  $\Delta M_{\text{bol}}(15)$ , which displays a significantly more scatter, extending to tens of percents. The greater precision of our sample is partly due to the choice of the shape parameter and partly due to the data quality and analysis, as our relation using  $\Delta M_{\text{bol}}(15)$  (see Section 4.1) is tighter than the relation in Scalzo et al. (2019).

The results of the models resemble those of the  $t_0$ - $M_{\text{Ni}56}$  distribution (Figure 2), where none of the models reproduce the positive correlation in the  $L_{30}/L_p$ - $L_p$  relation across the entire luminosity range.

The Chandra models, represented by the green line, overlap with the observations only in a limited region. Unlike the observed relation, these models exhibit a distinct negative correlation across most luminosity ranges. The faint models are much slower than observed, while the bright models are faster.

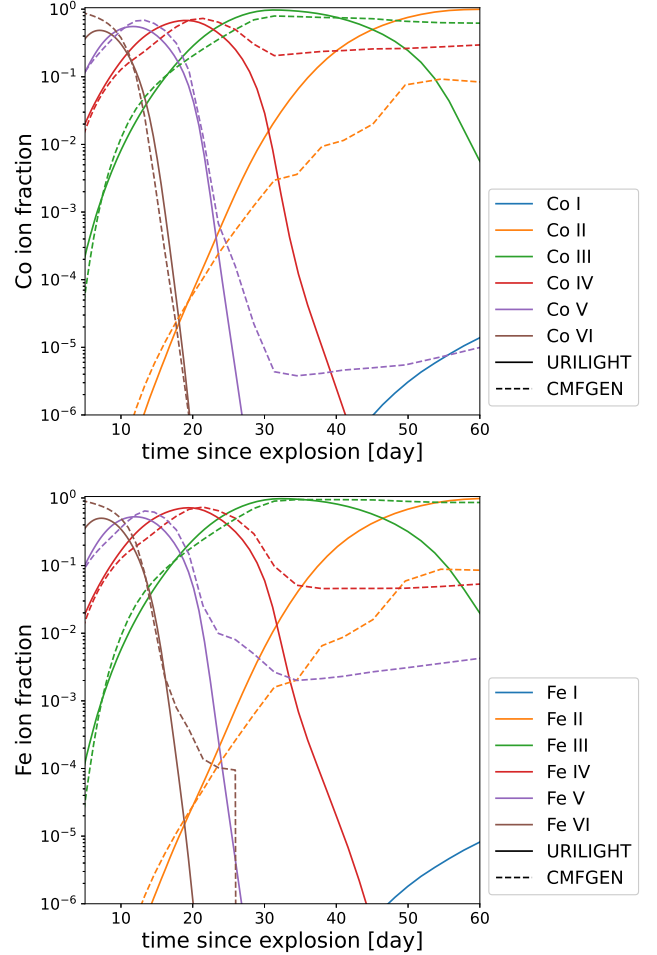


**Figure 5.** Temporal evolution of the mean Co (top) and Fe (bottom) ionization levels in the toy06 model, depicted for URILIGHT (solid lines) and CMFGEN (dashed lines). The ionization levels show good agreement up to  $\approx 30$  days from the explosion, after which they diverge. This is attributed to the epoch when ionization from non-thermal leptons becomes significant.

The 1D sub-Chandra models, depicted by the red line, align well with low-luminosity SNe. However, the  $L_{30}/L_p$  values for the more luminous SNe show significant tension with the observations. Notably, the more luminous SNe Ia, corresponding to  $^{56}\text{Ni}$  masses of  $M_{\text{Ni}56} \gtrsim 0.5 M_{\odot}$  and  $L_p \gtrsim 1.2 \times 10^{43} \text{ erg s}^{-1}$ , encompass the vast majority of events (Sharon & Kushnir 2022). The results for the off-centered ignitions of sub-Chandra WDs are shown for WD masses of 0.8, 0.85, 0.9, 0.95, 1, 1.1  $M_{\odot}$  and ignition locations of  $z_{\text{ig}} = 0, 0.1, 0.25, 0.5$ . These results are presented for different values of the inclination angle  $\theta$ , distributed evenly in  $\cos \theta$ , along with the angle-averaged values. The  $z_{\text{ig}} = 0$  configurations slightly deviate from their 1D counterparts due to 2D instabilities in the thermonuclear detonation wave (see Schinasi-Lemberg & Kushnir 2024, for a detailed discussion).

The models with  $z_{\text{ig}} > 0$  show significant variations due to the inclination angle, with a spread of up to  $\approx 25$  percent in  $L_{30}/L_p$  and  $\approx 50$  percent in  $L_p$  for the most asymmetric configurations. These variations are more pronounced for high masses, displaying a clear anti-correlation between the parameters. For  $M \lesssim 0.85, M_{\odot}$ , the observables are only marginally influenced by the inclination angle. Our results generally align with the non-spherical sub-Chandra

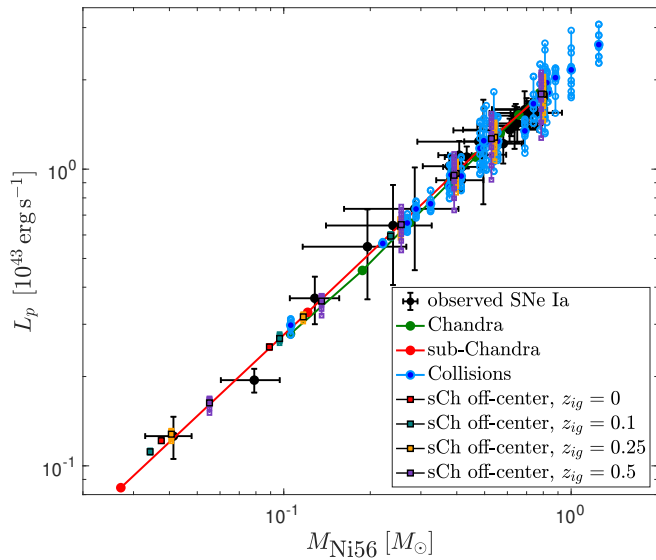


**Figure 6.** Comparison between the  $^{56}\text{Ni}$  mass,  $M_{\text{Ni}56}$ , to the peak luminosity,  $L_p$ , for the observed sample and explosion models. The symbols are the same as in Figure 1. The two parameters have an almost perfect correlation.

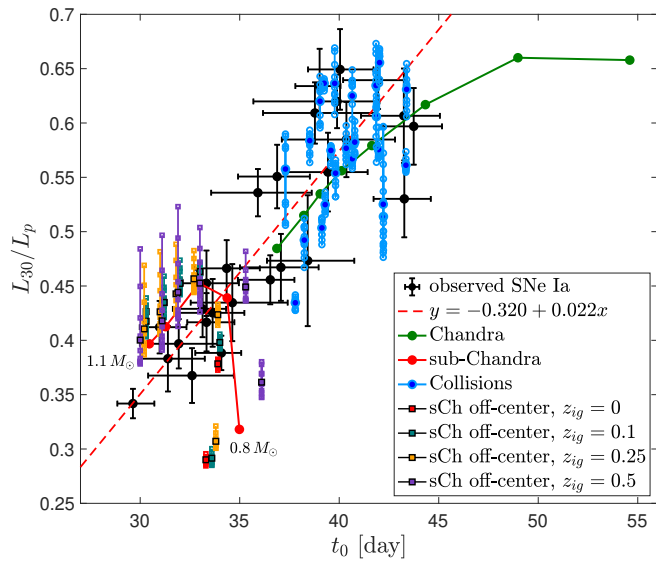


**Figure 7.** Same as Figure 6 but for the  $\gamma$ -ray escape time,  $t_0$ , and  $L_{30}/L_p$ . For the sub-Chandra models, the lowest and highest progenitor mass is displayed near their respective values. The parameters exhibit strong correlations in both the observations and the models, except for the sub-Chandra detonations. These models show a decrease of  $L_{30}/L_p$  for the high  $t_0$  values, corresponding to low-mass WD progenitors. This drop is related to the short rise times of these models; see the main text for a detailed discussion. We also fit a linear regression model to the observed sample (dashed red line), and we find a slope of  $\approx 0.022 \text{ day}^{-1}$ .

explosions presented by Shen et al. (2021b). However, their findings show larger variations in the shape parameter, particularly for low-mass configurations. Compared to the 1D sub-Chandra models, the off-centered detonation results cover a larger fraction of the  $L_{30}/L_p - L_p$  distribution and account for some of the observed spread. Nonetheless, they fail to reproduce the  $L_{30}/L_p - L_p$  positive correlation for the luminous SNe, where the predicted  $L_{30}/L_p - L_p$  is smaller by  $\approx 25$  percent compared to observations.

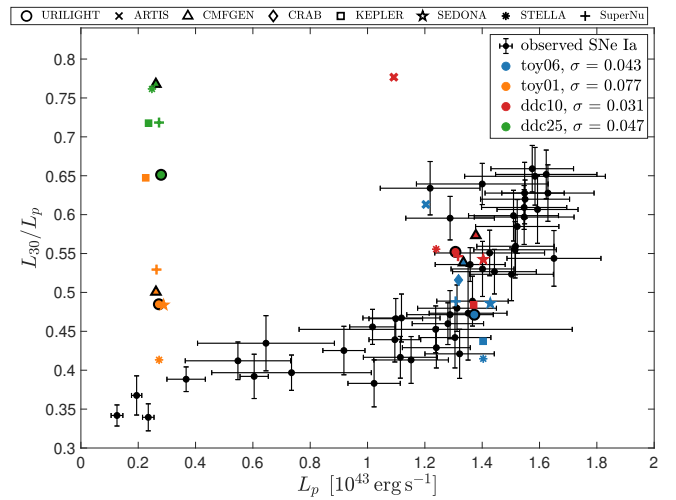


**Figure 8.** The  $L_p - L_{30}/L_p$  relation of the observed sample (black symbols) and the models from the StaNdaRT repository. The StaNdaRT results are represented by the colored symbols, with the colors and shapes corresponding to different explosion models and RT codes, respectively. The scatter in the  $L_{30}/L_p$  parameter between the RT codes for each explosion model (excluding ARTIS; see text for details) is provided in the legend.

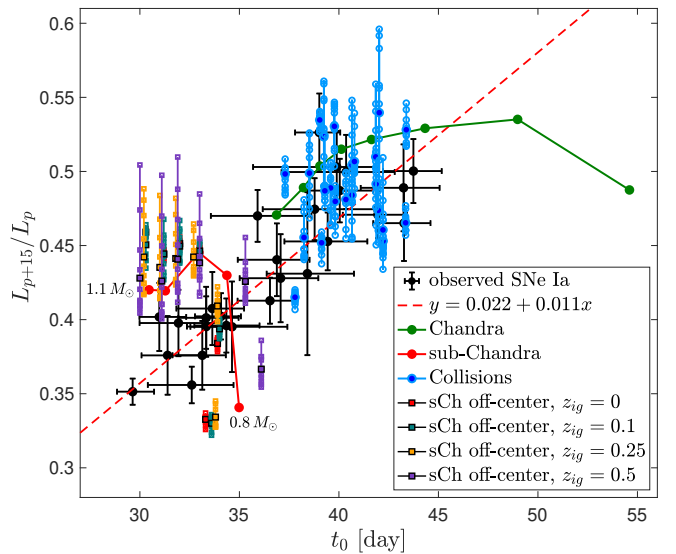


**Figure 9.** Same as Figure 7 but for the  $L_{p+15}/L_p - t_0$  relation. A version of this figure in magnitude space is provided in Appendix C.

The head-on WD collisions, observed at various inclination angles evenly distributed in  $\cos \theta$ , are represented by blue lines and circles, with dark blue circles indicating the angle-averaged values. The masses of each configuration are denoted in solar masses alongside their respective angle-averaged values or connected by lines. Configurations with equal masses exhibit reflection symmetry with respect to the plane perpendicular to the symmetry axis. Consequently, observables at angles  $\theta$  and  $-\theta$  are expected to align. Figure 1 confirms this alignment, albeit with slight variations due to Monte Carlo noise. These models can reproduce only the bright segment of the observed distribution. While models with intermediate masses achieve luminosities and shape parameters roughly consistent with observations, their luminosity varies significantly across different  $\theta$  values, often exceeding observed luminosities. The shape parameter

of these models is less sensitive to variations in the observed angle. The low-luminosity models exhibit high values of  $L_{30}/L_P$  compared to observations at similar luminosities and fail to match the observed relation across all  $\theta$  values. In these models, the observed inclination angle primarily affects  $L_{30}/L_P$ , altering it by up to  $\approx 20$  percent, which is insufficient to agree with the observed values. The relationship between the observed angle variations and the ejecta properties is a topic for future study.

In summary, none of the models can account for the observed  $L_{30}/L_P-L_P$  distribution.

#### 4.1 The $L_{P+15}/L_P-L_P$ relation

In Figure 10, we present the observed distribution of  $L_{P+15}/L_P$  and  $L_P$ . The general trend that lower luminosity SNe Ia evolve more rapidly is evident in this relationship. However, as noted in Section 3.2, the  $L_{P+15}/L_P$  parameter covers a smaller range of values, and the relation is not strictly monotonic, with some intermediate-luminosity objects displaying very high shape parameters.

The models' behavior mirrors that of the  $L_{30}/L_P-L_P$  relation, but the separation between the models is less pronounced. This is most apparent in the overlap between the high-luminosity sub-Chandrasekhar models and the collision models, which is also evident in the  $L_{P+15}/L_P-t_0$  relation (Figure 9). Here, sub-Chandrasekhar models exhibit  $L_{P+15}/L_P$  values that are higher than observed for SNe with low to intermediate luminosities, whereas the  $L_{30}/L_P-L_P$  relation better represented these SNe with the sub-Chandrasekhar models. Conversely, sub-Chandrasekhar models align more closely with the high luminosity regime, where most SNe Ia are situated. Results for viewing angles opposite the explosion point of more massive progenitors align with the most luminous objects. However, for viewing angles near the explosion point, the models predict too high luminosities that evolve more rapidly than observed data. A version of this figure in magnitude space is provided in Appendix C.

For the Chandra models, our findings are broadly consistent with those of Kasen & Woosley (2007), who derived light curves for Chandrasekhar-mass WD explosions and observed nearly constant  $\Delta M_{\text{bol}}(15)$  values across a  $M_{\text{Ni}56}$  range of  $0.35-0.7 M_{\odot}$ . In this luminosity range, our  $\Delta M_{\text{bol}}(15)$  results exhibit similar values but show variations of  $\approx 15$  percent.

## 5 OPACITY OF LOW-LUMINOSITY MODELS

We demonstrated in Section 3 that the sub-Chandra models exhibit a peculiar behavior in the low-luminosity region regarding the two shape parameters considered in this work,  $t_0$  and  $L_{30}/L_P$ . While  $t_0$  increases monotonically as the luminosity decreases,  $L_{30}/L_P$  does not follow a monotonic trend across all luminosities and reverses for the two faintest models. This anti-correlation is evident in Figure 7, where  $L_{30}/L_P$  of the sub-Chandra models drops for high values of  $t_0$ , corresponding to the fainter models of the  $0.8$  and  $0.85 M_{\odot}$  WD progenitors. The drop in  $L_{30}/L_P$  is attributed to the short rise time evident in these models. Since both the rise time and the  $\gamma$ -ray escape time are expected to increase with the ejecta's mass and decrease with the kinetic energy of the ejecta and the extent of the  $^{56}\text{Ni}$  distribution within it, this suggests that the anti-correlation is likely due to opacity differences.

As discussed in the preceding sections, the opacity of optical light, which depends on the temperature, density, and composition of the matter, significantly impacts the evolution of the SNe light curve.

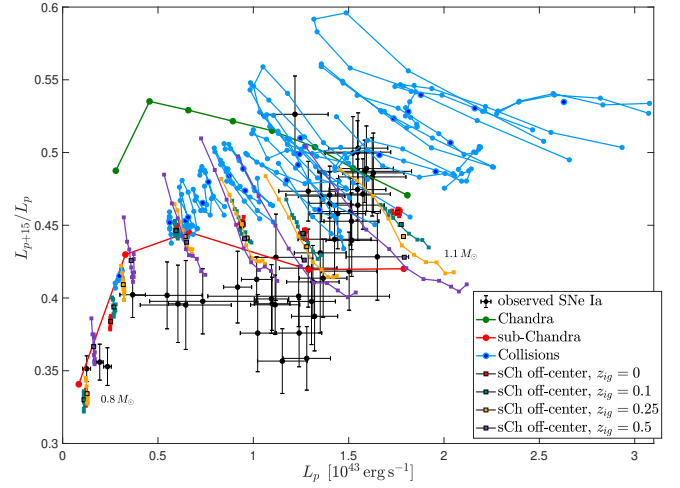


**Figure 10.** Same as Figure 1, but for the  $L_{P+15}/L_P-L_P$  distribution. Compared to Figure 1, the  $L_{P+15}/L_P$  shape parameter covers a smaller range of values and is not strictly monotonic with the luminosity. Additionally, the models are not as well separated, which is most evident in the overlap between the sub-Chandrasekhar and collision models. A version of this figure in magnitude space is provided in Appendix C.

In contrast, the opacity for  $\gamma$ -ray transfer is almost constant for the ejecta considered here. Therefore, we evaluate and compare the characteristic optical opacity of the models. This is not straightforward, as optical opacity is wavelength-dependent, varies throughout the ejecta, and evolves over time. To address the wavelength dependency, we use the Rosseland mean opacity since the photons travel through diffusion during the early stages of the SN. For each epoch, we calculate the mass-averaged Rosseland mean opacity:

$$\langle \kappa_R(t) \rangle = \frac{1}{m_*} \int_0^{m_*(t)} \kappa_R dm, \quad (3)$$

where  $m_*(t)$  is the enclosed mass within which the diffusion approximation is valid, determined by an optical depth from the ejecta outer edge of  $\tau > 2$ .

The temporal evolution of the mass-averaged Rosseland mean opacity for several selected models is shown in Figure 11, with the epoch of peak light for each model marked by a black point. The sub-Chandra models, represented by solid lines, exhibit a significant decrease in average opacity for the low-mass progenitors compared to other models. This decrease is particularly pronounced in the  $0.8 M_{\odot}$  model, which has substantially lower opacities – nearly half as much around peak light – compared to the other models. The opacities of the faintest and brightest Chandra models, indicated by the dashed lines, also show significant variation.

The opacity variations observed for both the sub-Chandra and Chandra models are consistent with their behavior in Figure 7. These variations explain the short rise times of the low-luminosity sub-Chandra models despite their relatively high  $t_0$  values. In Appendix B, we provide a quantitative analysis of these results and directly relate the models' rise time to their average Rosseland mean opacity.

## 6 SUMMARY AND CONCLUSIONS

In this study, we aimed to identify an observational width–luminosity relation, similar to the  $t_0-M_{\text{Ni}56}$  relation, that would allow to constrain multi-D models at pre-nebular phases while minimizing the

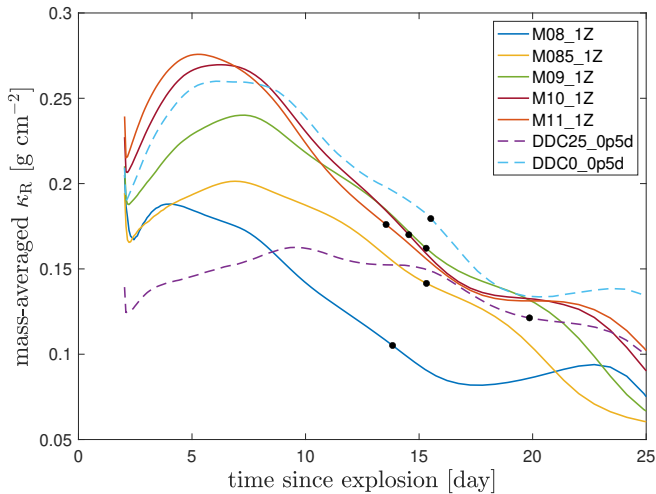


**Figure 11.** Mass-averaged Rosseland mean opacity as a function of time for several selected models. The models include the 1D sub-Chandra configurations (solid lines) and the two Chandra models with the faintest and brightest luminosities (dashed lines). The black point on each curve indicates the epoch of peak light. Averaging was performed over all masses with an optical depth from the outer edge of the ejecta satisfying  $\tau > 2$ . The opacity of the  $0.8 M_{\odot}$  WD sub-Chandra model is significantly lower than the other models, consistent with its short rise time.

inherent uncertainties of RT calculations. We argued that the bolometric light curve up to 30 days from the explosion can be computed without accounting for NLTE effects, which are inherently uncertain and difficult to compute (Section 3). Subsequently, we introduced a width-luminosity relation for SNe Ia, where the peak luminosity  $L_p$  is compared with the ratio of the luminosity at 30 days from the explosion to the peak luminosity,  $L_{30}/L_p$ . The distribution of these parameters for a sample of 47 SNe Ia is presented in Figure 1, along with the results from 1D and 2D explosion models (see Section 4).

In previous work, we compared the observed  $t_0-M_{\text{Ni}56}$  relation to known SNe Ia models from the literature (Sharon & Kushnir 2020a, also see Figure 2 for an updated relation). Although that analysis bypassed RT calculations, it could not account for multi-D effects and required stringent observational conditions, including late-time observations up to  $\sim 100$  days. While the current analysis relies on RT calculations, it does not face these limitations. The conclusion of this work aligns with that of Sharon & Kushnir (2020a): None of the known SNe Ia models can reproduce the observed width-luminosity distribution of SNe Ia, even when considering multi-D effects.

Several avenues could potentially align the models more closely with the observations. One possibility involves adjusting the initial composition of the sub-Chandra WDs, which evolve too rapidly compared to the bulk of the observations, from CO towards heavier elements. This adjustment would reduce the available thermonuclear energy of the WD, resulting in lower velocities of the ejected material and a slower evolution of the light curve. However, a heavier composition is expected only for very massive WDs (Laufer et al. 2018,  $M \gtrsim 1.1 M_{\odot}$ ). We are currently investigating this possibility, and the findings will be published in a subsequent work.

Another avenue is to perform more accurate calculations of the collision model. The calculations by Kushnir et al. (2013) were carried out with relatively low resolution and a simplified 13-isotope reaction network. Preliminary results from more accurate calculations do not show a substantial change in the  $L_{30}/L_p-L_p$  distribution and will be reported in a future paper. Additionally, 3D calculations of colli-

sions with non-zero impact parameters could yield different results; however, such high-resolution calculations are currently beyond our computational capabilities.

Throughout the paper, we have mentioned non-thermal processes as significant sources of uncertainty in RT modeling. These processes substantially impact the SN’s evolution, yet their full extent and impact remain poorly understood. Traditionally, non-thermal effects are primarily considered during the nebular phase; however, Dessart et al. (2012) demonstrated that non-thermal excitation alters the spectra of Type Ib SNe, even at earlier phases, during the photospheric phase. Therefore, it is crucial to understand their impact on pre-nebular times and the SN light curves. Furthermore, parameters associated with non-thermal processes contain considerable uncertainties. For example, electron-impact ionization cross-sections are often unknown, and the absence of such cross-sections for Co III ionization in CMFGEN causes substantial discrepancies in Co and Fe ionization levels, as illustrated in Figure 5. Future work should study in more detail the effect non-thermal processes have on the SNe observables and their sensitivity to the non-thermal parameters.

## ACKNOWLEDGEMENTS

We thank Boaz Katz for offering this work and for the useful discussions. We thank Stéphane Blondin and John Hillier for their assistance regarding CMFGEN. DK is supported by a research grant from The Abramson Family Center for Young Scientists, and by the Minerva Stiftung.

## DATA AVAILABILITY

The data underlying this article are available in the article and in its online supplementary material.

## REFERENCES

- Arnaud M., Rothenflug R., 1985, *A&AS*, **60**, 425  
 Axelrod T. S., 1980, PhD thesis, University of California, Santa Cruz  
 Baron E., Hauschildt P. H., Nugent P., Branch D., 1996, *MNRAS*, **283**, 297  
 Blinnikov S. I., Bartunov O. S., 1993, *A&A*, **273**, 106  
 Blondin S., Dessart L., Hillier D. J., Khokhlov A. M., 2017, *MNRAS*, **470**, 157  
 Blondin S., et al., 2022, *A&A*, **668**, A163  
 Burns C. R., et al., 2018, *ApJ*, **869**, 56  
 Chen N. M., et al., 2023, *ApJ*, **944**, L28  
 Collins C. E., Gronow S., Sim S. A., Röpke F. K., 2022, *MNRAS*, **517**, 5289  
 Contardo G., Leibundgut B., Vacca W. D., 2000, *A&A*, **359**, 876  
 Contreras C., et al., 2010, *AJ*, **139**, 519  
 Dessart L., Hillier D. J., 2010, *MNRAS*, **405**, 2141  
 Dessart L., Hillier D. J., Li C., Woosley S., 2012, *MNRAS*, **424**, 2139  
 Dessart L., Blondin S., Hillier D. J., Khokhlov A., 2014, *MNRAS*, **441**, 532  
 Gronow S., Collins C. E., Sim S. A., Röpke F. K., 2021, *A&A*, **649**, A155  
 Guttman O., Shenhar B., Sarkar A., Waxman E., 2024, *arXiv e-prints*, p. arXiv:2403.08769  
 Hillebrandt W., Niemeyer J. C., 2000, *ARA&A*, **38**, 191  
 Hillier D. J., Miller D. L., 1998, *ApJ*, **496**, 407  
 Jeffery D. J., 1999, arXiv preprint astro-ph/9907015  
 Jerkstrand A., 2011, PhD thesis, Stockholm University  
 Kasen D., 2006, *ApJ*, **649**, 939  
 Kasen D., Woosley S. E., 2007, *ApJ*, **656**, 661  
 Kasen D., Thomas R. C., Nugent P., 2006, *ApJ*, **651**, 366  
 Kozma C., Fransson C., 1992, *ApJ*, **390**, 602  
 Krisciunas K., et al., 2017, *AJ*, **154**, 211

- Kushnir D., Katz B., 2019, *Research Notes of the American Astronomical Society*, **3**, 162
- Kushnir D., Katz B., Dong S., Livne E., Fernández R., 2013, *ApJ*, **778**, L37
- Kushnir D., Wygoda N., Sharon A., 2020, *MNRAS*, **499**, 4725
- Kwok L. A., et al., 2023, *ApJ*, **944**, L3
- Lauffer G. R., Romero A. D., Kepler S. O., 2018, *MNRAS*, **480**, 1547
- Li C., Hillier D. J., Dessart L., 2012, *MNRAS*, **426**, 1671
- Maiz D., Mannucci F., Nelemans G., 2014, *ARA&A*, **52**, 107
- Nahar S. N., 1996, *Phys. Rev. A*, **53**, 2417
- Noebauer U. M., Sim S. A., 2019, *Living Reviews in Computational Astrophysics*, **5**, 1
- Phillips M. M., 1993, *ApJ*, **413**, L105
- Phillips M. M., Lira P., Suntzeff N. B., Schommer R. A., Hamuy M., Maza J., 1999, *AJ*, **118**, 1766
- Phillips M. M., et al., 2006, *AJ*, **131**, 2615
- Riess A. G., et al., 2022, *ApJ*, **934**, L7
- Scalzo R., et al., 2014, *MNRAS*, **440**, 1498
- Scalzo R. A., et al., 2019, *MNRAS*, **483**, 628
- Schinasi-Lemberg E., Kushnir D., 2024, in preparation
- Sharon A., Kushnir D., 2020a, *Research Notes of the American Astronomical Society*, **4**, 158
- Sharon A., Kushnir D., 2020b, *MNRAS*, **496**, 4517
- Sharon A., Kushnir D., 2022, *MNRAS*, **509**, 5275
- Sharon A., Kushnir D., 2023, *MNRAS*, **522**, 6264
- Shen K. J., Blondin S., Kasen D., Dessart L., Townsley D. M., Boos S., Hillier D. J., 2021a, *ApJ*, **909**, L18
- Shen K. J., Boos S. J., Townsley D. M., Kasen D., 2021b, *ApJ*, **922**, 68
- Shingles L. J., et al., 2020, *MNRAS*, **492**, 2029
- Shingles L. J., Flörs A., Sim S. A., Collins C. E., Röpke F. K., Seitzzahl I. R., Shen K. J., 2022, *MNRAS*, **512**, 6150
- Shull J. M., van Steenberg M., 1982, *ApJS*, **48**, 95
- Sim S. A., Röpke F. K., Hillebrandt W., Kromer M., Pakmor R., Fink M., Ruiter A. J., Seitzzahl I. R., 2010, *ApJ*, **714**, L52
- Stritzinger M., Leibundgut B., Walch S., Contardo G., 2006, *A&A*, **450**, 241
- Stritzinger M. D., et al., 2011, *AJ*, **142**, 156
- Utrobin V. P., 2004, *Astronomy Letters*, **30**, 293
- Wollaeger R. T., van Rossum D. R., Graziani C., Couch S. M., Jordan George C. I., Lamb D. Q., Moses G. A., 2013, *ApJS*, **209**, 36
- Woolsey S. E., Heger A., Weaver T. A., 2002, *Reviews of Modern Physics*, **74**, 1015
- Wygoda N., Elbaz Y., Katz B., 2019a, *MNRAS*, **484**, 3941
- Wygoda N., Elbaz Y., Katz B., 2019b, *MNRAS*, **484**, 3951

## APPENDIX A: EMERGENCE OF NON-THERMAL IONIZATION

In this appendix, we use simple analytic arguments to estimate the epoch at which the ionization rate from non-thermal leptons becomes significant, leading to a departure from LTE for the ionization levels. The ionization fraction  $x_i$  for a given element at ionization level  $i$  is determined from the equation (Jerkstrand 2011)

$$\frac{dx_i}{dt} = \Gamma_{\text{ion},i-1}x_{i-1} + \Gamma_{\text{rec},i+1}x_{i+1} - (\Gamma_{\text{ion},i}x_i + \Gamma_{\text{rec},i}x_i), \quad (\text{A1})$$

where  $\Gamma_{\text{ion},i}$  and  $\Gamma_{\text{rec},i}$  are the total ionization and recombination rates per particle from level  $i$ , respectively. Since the ionization and the recombination time scales are much shorter than the dynamical time, we look for the steady-state solution:

$$\Gamma_{\text{ion},i}x_i = \Gamma_{\text{rec},i+1}x_{i+1}. \quad (\text{A2})$$

At early times, when non-thermal effects are still negligible and the ionization levels are at their LTE values, the ionization rate is primarily due to photoionization. As the ejecta expands and cools, non-thermal ionization caused by the impact of fast leptons will start

to dominate once its rate becomes comparable to the recombination rate.

To estimate the time when non-thermal ionization becomes significant, we examine the state of the iron-group elements in the ejecta's core, composed of Ni, Co, and Fe. For simplicity, we consider only Fe ionization levels in what follows. We assume that the iron in the ejecta is composed only of Fe III and Fe IV, with relative abundances  $x_{\text{III}}$  and  $x_{\text{IV}} = 1 - x_{\text{III}}$ , respectively. These are the two dominant ions after 20 days from the explosion, as seen in Figure 5. The epoch  $t_{\text{eq}}$  when the non-thermal ionization rate becomes significant is estimated by

$$\Gamma_{\text{ion}}^{\text{nt}}(t_{\text{eq}})x_{\text{III}}(t_{\text{eq}}) = \Gamma_{\text{rec}}(t_{\text{eq}})x_{\text{IV}}(t_{\text{eq}}), \quad (\text{A3})$$

where  $\Gamma_{\text{ion}}^{\text{nt}}$  is the non-thermal ionization rate per particle for Fe III,  $\Gamma_{\text{rec}}$  is the recombination rate per particle for Fe IV, and the ionization levels correspond to their LTE evolution within the ejecta. We now estimate the recombination and ionization rate per particle of these ions.

Assuming that recombination is primarily from free electrons within the considered temperature range (Jerkstrand 2011), the recombination rate is given by

$$\Gamma_{\text{rec}}(t) = \alpha n_e(t), \quad (\text{A4})$$

where  $\alpha$  is the temperature-dependent recombination coefficient and  $n_e$  is the electron density. At a temperature of  $T \sim 10^4$  K, typical for the ejecta environment  $\approx 30$  days after explosion,  $\alpha \sim 1-5 \times 10^{-12} \text{ cm}^3 \text{ s}^{-1}$  for doubly- or triply-ionized iron-group ions (Shull & van Steenberg 1982; Nahar 1996; Jerkstrand 2011). The electron density is given by

$$n_e = \chi_e n_{\text{ion}} = \chi_e \frac{1}{A} \frac{M_{\text{core}}}{m_p} \frac{3}{4\pi(v_{\text{ej}} \cdot t)^3}, \quad (\text{A5})$$

where  $\chi_e$  is the mean number of free electrons per atom,  $n_{\text{ion}}$  is the ion density,  $A = 56$  is the atomic mass number,  $m_p$  is the proton mass,  $M_{\text{core}}$  is the total mass of the core, and  $v_{\text{ej}}$  is the characteristic velocity of the ejecta's core. Assuming the degree of ionization is similar for different elements in the ejecta, then  $\chi_e = 2x_{\text{III}} + 3x_{\text{IV}}$ . Unless large amounts of non-radioactive isotopes (e.g.,  $^{54}\text{Fe}$ ) are produced in the explosion,  $M_{\text{core}} \approx M_{\text{Ni56}}$ , so we use  $M_{\text{Ni56}}$  to denote the core mass in what follows.

To estimate the non-thermal ionization rate, we assume that a fraction  $\eta_{\text{ion}}$  of the energy of the fast leptons is converted into ionization of the ions, while the remaining energy goes into heating of the free electrons and excitation of bound electrons. The value of  $\eta_{\text{ion}}$  depends primarily on the fraction of free electrons and the composition and only weakly on the number densities. For SNe Ia ejecta,  $\eta_{\text{ion}} \approx 0.02 - 0.2$  (Kozma & Fransson 1992; Dessart et al. 2012; Li et al. 2012; Shingles et al. 2022). Assuming, for simplicity, that the energy for non-thermal ionization is distributed among the elements and ions in proportion to their relative abundance due to similar cross sections (Arnaud & Rothenflug 1985), the non-thermal ionization rate per particle will be

$$\Gamma_{\text{ion}}^{\text{nt}}(t) = \eta_{\text{ion}} \frac{Q_{\text{dep}}(t)}{I_{\text{III}} \cdot N_{\text{ion}}} = \eta_{\text{ion}} \frac{Q_{\text{dep}}(t)}{M_{\text{Ni56}}} \frac{m_p A}{I_{\text{III}}}, \quad (\text{A6})$$

where  $Q_{\text{dep}}(t)$  is the total energy deposition of the radioactive decay,  $I_{\text{III}} = 30.65$  eV is the Fe III ionization energy,  $N_{\text{ion}}$  is the total number of ions, and it is assumed that all radioactive energy is deposited in the core. The term  $\tilde{Q}_{\text{dep}}(t) \equiv Q_{\text{dep}}(t)/M_{\text{Ni56}}$  is independent of  $M_{\text{Ni56}}$ , varying only due to differences in the  $\gamma$ -ray deposition fraction. For the observed range of  $\gamma$ -ray escape times of SNe Ia,  $t_0 \approx 30 - 45$  day (Sharon & Kushnir 2020b), the range of  $\tilde{Q}_{\text{dep}}(30 \text{ day})$  varies by

at most  $\approx 30$  percent. Plugging in the expressions for the rates in Equation (A3), and using  $x_{\text{III}} = 1 - x_{\text{IV}}$ , we get

$$t_{\text{eq}}^3 \tilde{Q}_{\text{dep}}(t_{\text{eq}}) = \frac{3}{4\pi v_{\text{ej}}^3} \frac{\alpha M_{\text{Ni56}} I_{\text{III}}}{\eta_{\text{ion}}} \left( \frac{1}{A m_p} \right)^2 (2 + x_{\text{IV}}) \frac{x_{\text{IV}}}{1 - x_{\text{IV}}}. \quad (\text{A7})$$

We next demonstrate that Equation (A7) is consistent with  $t_{\text{eq}} \approx 30$  days observed in Section 3 for the toy06 model from Blondin et al. (2022). For the toy06 model, we find  $\tilde{Q}_{\text{dep}}(t) \approx \tilde{Q}_{\text{dep}}(t = 30 \text{ day}) \approx 1.03 \times 10^{43} \frac{\text{erg s}^{-1}}{M_{\odot}}$ , with  $\approx 90$  percent of this energy deposited in the core. Using  $\alpha = 5.1 \times 10^{-12} \text{ cm}^3 \text{ s}^{-1}$  for Fe IV recombination (Nahar 1996), we get

$$t_{\text{eq}} \approx \left( \frac{0.05}{\eta_{\text{ion}}} \right)^{1/3} \left( \frac{M_{\text{Ni56}}}{0.6 M_{\odot}} \right)^{1/3} \left( \frac{0.55 \times 10^9 \text{ cm s}^{-1}}{v_{\text{ej}}} \right) \times \frac{1}{0.38} \left[ \left( 1 + \frac{x_{\text{IV}}}{2} \right) \frac{x_{\text{IV}}}{1 - x_{\text{IV}}} \right]^{1/3} \times 31.5 \text{ day}, \quad (\text{A8})$$

where we use the core mass ( $M_{\text{Ni56}} = 0.6 M_{\odot}$ ) and ejecta velocity values ( $v = 0.55 \times 10^9 \text{ cm s}^{-1}$ ) of the toy06 model, and normalize for  $x_{\text{IV}} = 0.05$  (the term in the square brackets and the value preceding it cancel out for this value), which marks the onset where Fe ionization in the toy06 model diverges from LTE (Figure 5). The good agreement with Figure 5 supports our simplified description of the deviation from LTE. Note the weak dependence of  $t_{\text{eq}}$  to the model parameters, except for  $v_{\text{ej}}$  with linear dependence.

For a more accurate treatment, we present in Figure A1 solutions of Equation (A7) for several  $\eta_{\text{ion}}$  values, shown as red lines. The  $^{56}\text{Ni}$  mass, velocity, and deposition fraction are that of the toy06 model. The temperature is assumed to remain constant at  $10^4 \text{ K}$ , thereby maintaining the recombination coefficient constant. The solid and dashed black curves trace the evolution of  $x_{\text{IV}}$  in the URILIGHT and CMFGEN codes, respectively, for the toy06 model. The intersection between the solution of Equation (A7) and the LTE evolution of  $x_{\text{IV}}$  marks the epoch where non-thermal ionization equals the recombination rate, becoming non-negligible. As illustrated in Figure A1,  $x_{\text{IV}}$  drops rapidly within a narrow time range, occurring between 25 to 35 days from the explosion. Consequently, the value of  $t_{\text{eq}}$  at the intersection has a weak dependence on the parameters of Equation (A7). Figure A1 also shows that these intersection times are consistent with the departure of  $x_{\text{IV}}$  from LTE value, as evidenced by its evolution simulated with CMFGEN.

For completeness, we perform the same analysis for the low-luminosity model toy01. We replace the model parameters such that the  $^{56}\text{Ni}$  mass and velocity are  $M_{\text{Ni56}} = 0.1 M_{\odot}$ ,  $v = 0.24 \times 10^9 \text{ cm s}^{-1}$ . In addition, due to the model's low core mass, the energy deposition  $\tilde{Q}_{\text{dep}}$  takes into account that a lower fraction of the energy deposition goes into the core, around  $\approx 65$  percent, than in the toy06 model. The results for the toy01 model are shown in Figure A2, and are also consistent with the departure of  $x_{\text{IV}}$  from its LTE value slightly before 30 days.

## APPENDIX B: COMPARISON OF THE RISE TIME TO ANALYTIC RESULTS

In this appendix, we relate the rise time of our 1D models to the opacity of the ejecta. For this purpose, we use the analytical results of (Kushnir & Katz 2019, hereafter analytical results), which provide a solution for diffusion in an isotropic, homologously expanding ejecta, under radiation-dominated pressure, uniform density and opacity,  $\kappa$ , and local energy deposition from radioactive decay. Following the

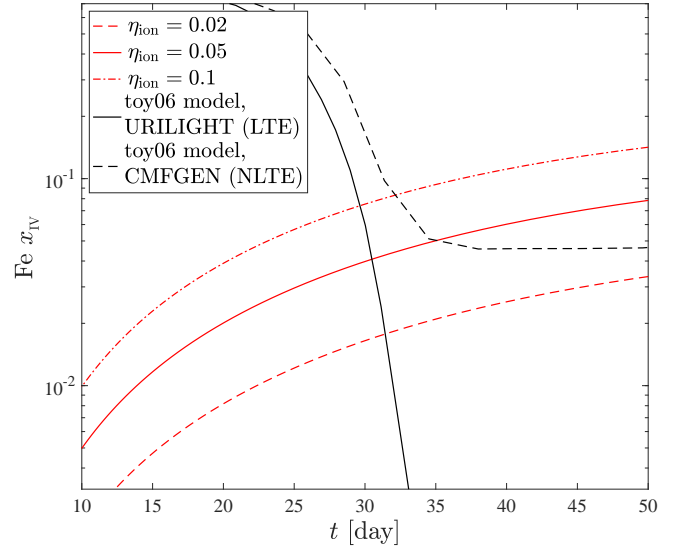


**Figure A1.** The evolution of the Fe IV fraction,  $x_{\text{IV}}$ , over time where non-thermal electron ionization equals the recombination rate (red lines), calculated using Equation (A7) with parameters specific to the toy06 model. Various line styles represent different values of  $\eta_{\text{ion}}$ , governing the ionization fraction of non-thermal electron energy loss. The Fe IV evolution for the toy06 model simulated with URILIGHT and CMFGEN is indicated by solid and dashed black lines, respectively. The intersection marks the epoch when the non-thermal ionization rate begins to dominate over the thermal ionization rate.

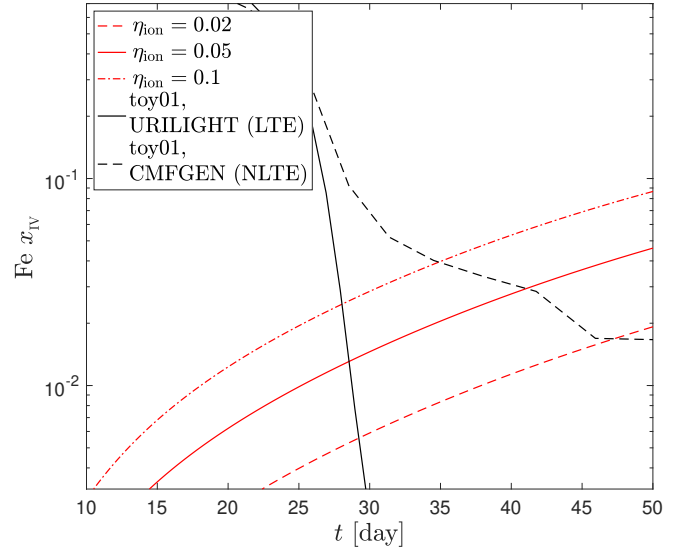


**Figure A2.** Same as Figure A1 but for the toy01 model. The results for this model are also consistent with the departure of  $x_{\text{IV}}$  from its LTE value occurring slightly before 30 days.

methods in Kushnir & Katz (2019), the luminosity emitted from the ejecta can be calculated for a given ejecta mass  $M$ , outer velocity  $v_o$ , opacity  $\kappa$ , and the extent of the energy generation region  $x_s$ , such that

$$\epsilon(v, t) = \frac{Q(t)}{\frac{4\pi}{3}(x_s v_o t)^3} \times \begin{cases} 1 & v < x_s v_o \\ 0 & \text{elsewhere} \end{cases}, \quad (\text{B1})$$

where  $\epsilon$  is the energy generation rate per unit volume and  $Q(t)$  is the total energy generation rate at time  $t$ . The resulting luminosity for an

impulse of energy  $E_\delta$  occurring at time  $t_\delta$  is given by

$$\frac{L_\delta(t; t_\delta)}{E_\delta} = \frac{t_\delta}{t_{\text{diff}}^2} \cdot \frac{6}{x_s^3} \sum_{n=1}^{\infty} (-1)^{n+1} \left( \frac{\sin(n\pi x_s)}{n\pi} - x_s \cos(n\pi x_s) \right) \times e^{-\frac{(n\pi)^2}{2t_{\text{diff}}^2}(t^2 - t_\delta^2)} \cdot u(t - t_\delta), \quad (\text{B2})$$

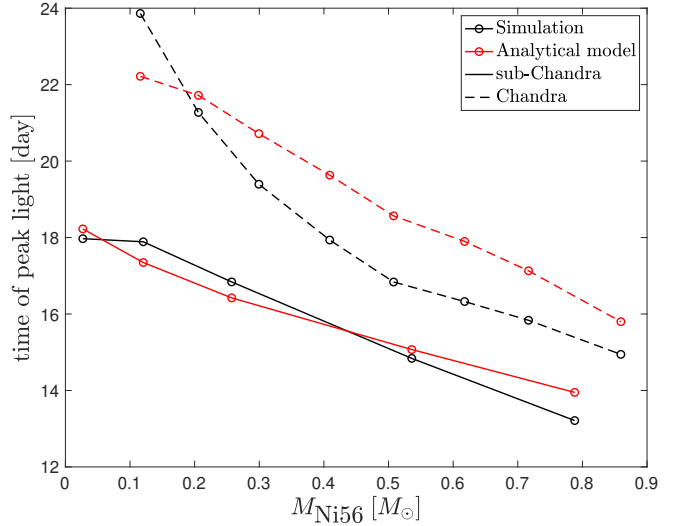
where  $t_{\text{diff}}^2 = 9\kappa M/4\pi v_o c$  and  $u$  is the Heaviside step function. The luminosity for a given energy generation rate  $Q(t)$  is

$$L(t) = \int_0^t dt' Q(t') L_\delta(t; t'). \quad (\text{B3})$$

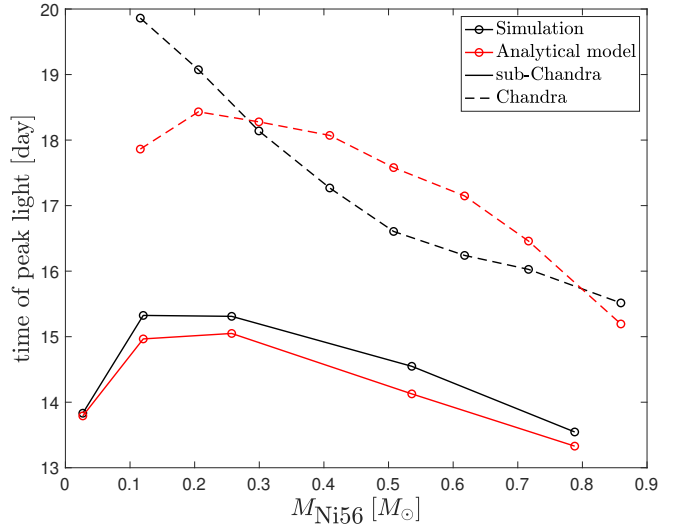
We proceed by comparing the analytical results with those obtained from our radiative transfer (RT) code, hereafter referred to as numerical or simulated results. Initially, we validate the analytical outcomes by simulating ejecta with uniform opacity and density, a constant volumetric energy generation rate, and local energy deposition without  $\gamma$ -ray transfer. Subsequently, we conduct simulations incorporating density profiles and  $^{56}\text{Ni}$  distributions specific to our models, incorporating  $\gamma$ -ray transfer while maintaining a uniform and constant opacity of  $0.2 \text{ g cm}^{-2}$ . To ensure consistency between the simulated and analytical models, we adjust the parameters of the analytical models — mass, velocity, and  $x_s$  — so that the ejecta mass, kinetic energy, and  $^{56}\text{Ni}$  mass remain conserved. For sub-Chandra models,  $x_s$  is determined such that the mass enclosed within  $x_s$  matches the  $^{56}\text{Ni}$  mass, given that these models exhibit a  $^{56}\text{Ni}$  distribution extending outward from the center. In contrast, for Chandra models where the central ejecta comprises non-radioactive intermediate-mass elements (IGEs) and  $^{56}\text{Ni}$  becomes dominant farther from the center, a single parameter  $x_s$  cannot fully characterize the  $^{56}\text{Ni}$  distribution. Therefore, we sum the total mass of IGE in the central regions until the radius where  $^{56}\text{Ni}$  becomes the dominant ion. We then determine the extent of the IGE in the analytical model,  $x_{\text{IGE}}$ , such that the enclosed mass within  $x_{\text{IGE}}$  equals the IGE mass at the center of the ejecta profile. The analytical model calculation involves energy generation occurring in the shell between  $x_{\text{IGE}}$  and  $x_s$ , ensuring that this shell's mass corresponds to the ejecta profile's  $^{56}\text{Ni}$  mass.

Figure B1 shows the rise times obtained from constant-opacity simulations (black lines) and analytical models (red lines) following the prescription above. As seen in the figure, the agreement between numerical and analytical results holds within a 10 percent margin for both sub-Chandra (solid lines) and Chandra (dashed lines) models. This robust agreement underscores the effectiveness of the analytical model. Additionally, the peak time consistently decreases with the SN luminosity across the entire range, mirroring the behavior of  $t_0$  for these models.

We proceed to compare the full numerical calculations with the analytical model, accounting for varying opacity in time and space within the simulations. To align the analytical model appropriately, we employ the mass-averaged Rosseland mean opacity (Equation (3)) at peak light,  $\langle \kappa_{\text{R}}(t_p) \rangle$ . The resulting opacities range from 0.1 to  $0.18 \text{ g cm}^{-2}$  for sub-Chandra models, and from 0.12 to  $0.18 \text{ g cm}^{-2}$  for Chandra models. In both models, the opacity increases monotonously with luminosity. The rise times derived from the analytical models using this approach are presented in Figure B2, alongside the simulation results. For sub-Chandra models, the analytical results (solid red line) closely match numerical calculations (solid black line) across the entire luminosity range, with deviations up to  $\approx 3$  percent. This robust agreement further underscores the influence of opacity variation on rise times and the  $L_{30}/L_p$  param-



**Figure B1.** Epoch of peak bolometric luminosity against the synthesized  $^{56}\text{Ni}$  mass, for configurations with a constant opacity of  $0.2 \text{ g cm}^{-2}$ . Black lines represent simulation results, while results from the analytic model of Kushnir & Katz (2019) are depicted in red. Solid lines correspond to sub-Chandra models, whereas dashed lines correspond to Chandra models. The parameters used in the analytical models are detailed in the text. For both models, the peak time shows a monotonic decrease with SN luminosity, consistent with the behavior of  $t_0$  for these models.



**Figure B2.** Same as Figure B1, but for full simulations, where opacity varies and is computed dynamically during the simulation. The opacity used in the analytical model is the mass-averaged Rosseland mean opacity derived from Equation (3), evaluated at peak light.

eter. Meanwhile, the analytical results (dashed red line) for Chandra models also align well with numerical calculations (dashed black line), albeit with deviations slightly larger, up to  $\approx 10$  percent.

## APPENDIX C: SOME RESULTS IN MAGNITUDE SPACE

Throughout this work, we used linear scaling for the luminosity and shape parameters we have presented. Here, we include additional graphs of some of our relations in magnitude space for completeness and comparison purposes. These are the  $\Delta M_{\text{bol}}(15)\text{-}t_0$  relation,

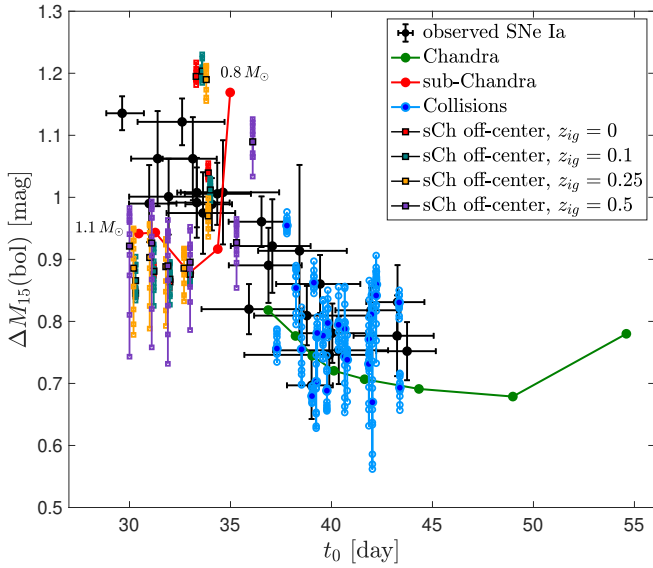


**Figure C1.** Same as Figure 9 but  $L_{p+15}/L_p$  is replaced with  $\Delta M_{\text{bol}}(15) = -2.5 \log(L_{p+15}/L_p)$ .

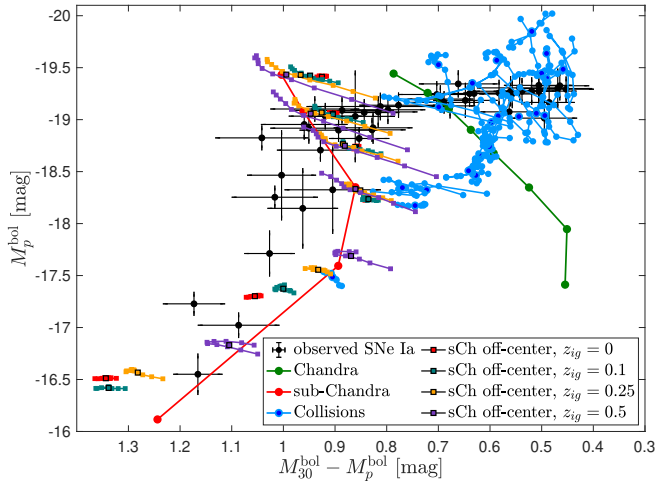


**Figure C2.** Same as Figure 1, but in magnitude space.

shown in Figure C1, and the  $L_{30}/L_p - L_p$  and  $L_{p+15}/L_p$  relations, shown in Figures C2 and 10, respectively.

#### APPENDIX D: PARAMETERS OF THE SNE SAMPLE AND OF THE MODELS

In this appendix, we outline the parameters utilized in our analysis. The characteristics of the observed sample can be found in Table D1, while the details of the models are provided in Table D2.

This paper has been typeset from a  $\text{\TeX}/\text{\LaTeX}$  file prepared by the author.

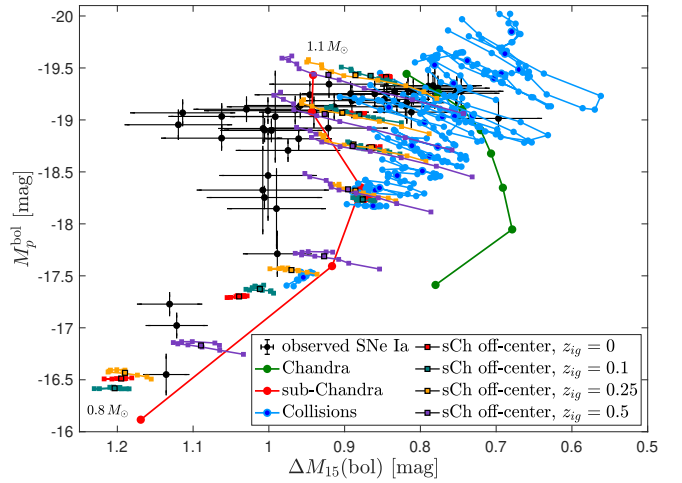


**Figure C3.** Same as Figure 10, but in magnitude space.

**Table D1.** Parameters of the SNe Ia sample.

name	$L_P$ ( $10^{43}$ erg s $^{-1}$ )	$L_{30}/L_P$	$\Delta M_{15}(\text{bol})$	$M_{\text{Ni56}}$ ( $M_{\odot}$ )	$t_0$ (day)	$t_0$ and $M_{\text{Ni56}}$ ref. <sup>a</sup>
2003du	1.36 ± 0.12	0.54 ± 0.02	0.82 ± 0.04	0.61 $^{+0.19}_{-0.15}$	35.91 $^{-2.35}_{-2.70}$	1
2004ef	1.10 ± 0.09	0.44 ± 0.03	1.00 ± 0.06	–	–	–
2004eo	1.12 ± 0.13	0.47 ± 0.03	0.92 ± 0.08	0.49 $^{-0.12}_{-0.10}$	37.07 $^{-2.06}_{-1.89}$	1
2004ey	1.51 ± 0.16	0.60 ± 0.03	0.84 ± 0.05	–	–	–
2004gs	0.92 ± 0.07	0.43 ± 0.03	0.97 ± 0.07	0.41 $^{-0.08}_{-0.08}$	33.64 $^{-1.81}_{-1.59}$	1
2005A	1.29 ± 0.15	0.60 ± 0.03	0.81 ± 0.05	–	–	–
2005M	1.63 ± 0.16	0.63 ± 0.04	0.78 ± 0.06	–	–	–
2005cf	1.43 ± 0.19	0.55 ± 0.03	0.89 ± 0.06	0.65 $^{-0.13}_{-0.14}$	36.88 $^{-1.96}_{-1.64}$	1
2005el	1.24 ± 0.48	0.45 ± 0.03	0.99 ± 0.06	0.49 $^{-0.20}_{-0.19}$	33.33 $^{-1.40}_{-1.35}$	1
2005hc	1.59 ± 0.14	0.61 ± 0.04	0.78 ± 0.07	0.70 $^{-0.17}_{-0.10}$	43.25 $^{-2.03}_{-1.81}$	2
2005iq	1.32 ± 0.12	0.42 ± 0.03	1.03 ± 0.07	–	–	–
2005kc	1.31 ± 0.14	0.48 ± 0.03	0.97 ± 0.07	–	–	–
2005ke	0.37 ± 0.07	0.39 ± 0.02	0.99 ± 0.04	0.13 $^{-0.02}_{-0.03}$	34.08 $^{-1.31}_{-1.00}$	1
2005ki	1.24 ± 0.12	0.43 ± 0.03	1.06 ± 0.07	0.48 $^{-0.05}_{-0.06}$	33.13 $^{-1.39}_{-1.18}$	1
2006D	1.11 ± 0.13	0.42 ± 0.03	1.01 ± 0.06	0.41 $^{-0.06}_{-0.04}$	33.33 $^{-0.97}_{-1.40}$	1
2006ax	1.44 ± 0.15	0.53 ± 0.03	0.85 ± 0.06	–	–	–
2006bh	1.15 ± 0.13	0.41 ± 0.03	1.12 ± 0.07	–	–	–
2006et	1.57 ± 0.14	0.66 ± 0.03	0.82 ± 0.06	–	–	–
2006kf	1.02 ± 0.09	0.38 ± 0.03	1.06 ± 0.08	0.38 $^{-0.07}_{-0.04}$	31.39 $^{-1.31}_{-0.85}$	1
2006mr	0.13 ± 0.02	0.34 ± 0.01	1.14 ± 0.03	0.04 $^{-0.01}_{-0.01}$	29.64 $^{-0.78}_{-1.08}$	2
2007N	0.19 ± 0.02	0.37 ± 0.03	1.12 ± 0.04	0.08 $^{-0.02}_{-0.02}$	32.61 $^{-2.21}_{-2.10}$	1
2007S	1.62 ± 0.18	0.65 ± 0.03	0.79 ± 0.06	–	–	–
2007af	1.02 ± 0.08	0.46 ± 0.02	0.96 ± 0.04	0.42 $^{-0.06}_{-0.07}$	36.54 $^{-1.63}_{-1.21}$	1
2007ba	0.60 ± 0.05	0.39 ± 0.03	1.01 ± 0.07	–	–	–
2007bc	1.31 ± 0.13	0.44 ± 0.04	1.00 ± 0.08	–	–	–
2007bd	1.28 ± 0.12	0.46 ± 0.03	1.11 ± 0.07	–	–	–
2007le	1.40 ± 0.23	0.64 ± 0.03	0.82 ± 0.04	0.64 $^{-0.16}_{-0.12}$	41.96 $^{-1.76}_{-1.46}$	1
2007on	0.55 ± 0.18	0.41 ± 0.02	0.99 ± 0.06	0.20 $^{-0.08}_{-0.07}$	30.98 $^{-1.00}_{-1.35}$	1
2008bc	1.55 ± 0.15	0.61 ± 0.03	0.81 ± 0.05	0.71 $^{-0.19}_{-0.11}$	38.78 $^{-2.61}_{-3.01}$	1
2008bf	1.52 ± 0.15	0.58 ± 0.03	0.75 ± 0.05	0.71 $^{-0.07}_{-0.11}$	40.36 $^{-3.24}_{-2.44}$	1
2008fp	1.58 ± 0.25	0.65 ± 0.04	0.78 ± 0.05	0.69 $^{-0.11}_{-0.14}$	40.04 $^{-2.44}_{-1.68}$	1
2008gp	1.50 ± 0.15	0.52 ± 0.03	0.95 ± 0.07	–	–	–
2008hj	1.52 ± 0.13	0.56 ± 0.04	0.89 ± 0.06	–	–	–
2008hv	1.10 ± 0.09	0.47 ± 0.03	1.01 ± 0.05	0.43 $^{-0.07}_{-0.06}$	34.34 $^{-1.61}_{-1.67}$	1
2009D	1.55 ± 0.14	0.63 ± 0.04	0.83 ± 0.06	–	–	–
2009F	0.24 ± 0.02	0.34 ± 0.02	1.13 ± 0.04	–	–	–
2009Y	1.55 ± 0.17	0.60 ± 0.04	0.75 ± 0.05	0.74 $^{-0.12}_{-0.13}$	43.74 $^{-1.53}_{-1.42}$	1
2009aa	1.37 ± 0.12	0.49 ± 0.03	0.96 ± 0.07	–	–	–
2009ab	1.29 ± 0.15	0.47 ± 0.03	0.94 ± 0.07	–	–	–
2009ad	1.65 ± 0.16	0.54 ± 0.04	0.92 ± 0.08	–	–	–
2011fe	1.22 ± 0.17	0.63 ± 0.03	0.70 ± 0.05	0.58 $^{-0.09}_{-0.09}$	39.02 $^{-1.22}_{-1.95}$	1
2012fr	1.40 ± 0.11	0.53 ± 0.04	0.83 ± 0.06	0.62 $^{-0.08}_{-0.09}$	43.27 $^{-1.94}_{-1.33}$	1
2012ht	0.65 ± 0.24	0.43 ± 0.04	1.01 ± 0.08	0.24 $^{-0.10}_{-0.09}$	34.63 $^{-2.09}_{-2.78}$	1
2013aa	1.51 ± 0.14	0.55 ± 0.04	0.86 ± 0.05	0.64 $^{-0.09}_{-0.08}$	39.44 $^{-2.17}_{-1.99}$	2
2015F	1.35 ± 0.14	0.47 ± 0.06	0.91 ± 0.14	0.54 $^{-0.15}_{-0.10}$	38.42 $^{-2.05}_{-2.34}$	1
2015bp	0.73 ± 0.28	0.40 ± 0.02	1.00 ± 0.06	0.29 $^{-0.12}_{-0.12}$	31.94 $^{-1.95}_{-2.04}$	2
2017cbv	1.55 ± 0.16	0.62 ± 0.02	0.75 ± 0.05	0.76 $^{-0.10}_{-0.17}$	39.89 $^{-4.20}_{-2.13}$	2

<sup>a</sup> Reference for the values of  $t_0$  and  $M_{\text{Ni56}}$ . (1) - Sharon & Kushnir (2020b). (2) - this work.

**Table D2.** Parameters of the models. For 2D models, the values for  $L_P$  and  $L_{30}/L_P$  represent angle-averaged results.

	name	$L_P$ ( $10^{43}$ erg s $^{-1}$ )	$L_{30}/L_P$	$\Delta M_{15}$ (bol) (mag)	$M_{\text{Ni}56}$ ( $M_{\odot}$ )	$t_0$ (d)
Chandra	DDC0_0p5d	0.28	0.66	0.78	0.11	54.60
	DDC10_0p5d	0.46	0.66	0.68	0.19	48.98
	DDC15_0p5d	0.66	0.62	0.69	0.27	44.33
	DDC17_0p5d	0.89	0.58	0.71	0.37	41.64
	DDC20_0p5d	1.10	0.56	0.72	0.47	40.12
	DDC22_0p5d	1.32	0.53	0.74	0.57	39.04
	DDC25_0p5d	1.52	0.51	0.78	0.66	38.22
	DDC6_0p5d	1.81	0.48	0.82	0.78	36.87
sub-Chandra, central ignition	M085_1Z	0.08	0.32	1.17	0.03	34.98
	M08_1Z	0.33	0.44	0.92	0.12	34.37
	M09_1Z	0.66	0.45	0.88	0.26	32.96
	M10_1Z	1.29	0.41	0.94	0.54	31.28
	M11_1Z	1.79	0.40	0.94	0.79	30.46
sub-Chandra, off-centered ignitions	M08_zig0	0.12	0.29	1.19	0.04	33.30
	M08_zig01	0.11	0.29	1.20	0.03	33.60
	M08_zig025	0.13	0.31	1.19	0.04	33.80
	M08_zig05	0.16	0.36	1.09	0.06	36.10
	M085_zig0	0.25	0.38	1.04	0.09	33.90
	M085_zig01	0.27	0.40	1.01	0.10	34.00
	M085_zig025	0.32	0.42	0.97	0.12	33.90
	M085_zig05	0.36	0.45	0.93	0.14	35.30
	M09_zig0	0.60	0.46	0.88	0.24	33.00
	M09_zig01	0.59	0.46	0.88	0.24	33.00
	M09_zig025	0.64	0.46	0.89	0.25	32.70
	M09_zig05	0.65	0.45	0.90	0.26	33.00
	M095_zig0	0.94	0.45	0.86	0.39	32.00
	M095_zig01	0.94	0.45	0.87	0.39	32.00
	M095_zig025	0.97	0.44	0.89	0.40	31.80
	M095_zig05	0.95	0.44	0.89	0.39	31.90
	M1_zig0	1.26	0.43	0.88	0.54	31.20
	M1_zig01	1.26	0.43	0.88	0.54	31.20
	M1_zig025	1.28	0.43	0.90	0.54	31.00
	M1_zig05	1.27	0.42	0.93	0.53	31.10
M11_zig0	1.76	0.43	0.85	0.80	30.30	
M11_zig01	1.78	0.42	0.87	0.80	30.30	
M11_zig025	1.79	0.41	0.89	0.80	30.20	
M11_zig05	1.79	0.40	0.92	0.79	30.00	
Head-on collisions	M05-M05	0.30	0.43	0.95	0.11	37.79
	M055-M055	0.56	0.50	0.86	0.22	39.13
	M07-M05	0.64	0.51	0.86	0.26	42.22
	M06-M05	0.66	0.49	0.85	0.27	38.25
	M08-M05	0.73	0.56	0.83	0.29	43.35
	M06-M06	0.76	0.55	0.80	0.32	39.82
	M07-M06	0.87	0.57	0.79	0.38	40.66
	M08-M06	0.96	0.58	0.81	0.38	41.97
	M064-M064	0.95	0.57	0.78	0.41	39.58
	M08-M07	1.18	0.58	0.79	0.48	40.35
	M09-M07	1.24	0.61	0.77	0.51	41.87
	M09-M06	1.25	0.63	0.73	0.50	41.85
	M07-M07	1.24	0.58	0.76	0.56	38.52
	M09-M05	1.35	0.53	0.84	0.69	42.21
	M09-M08	1.27	0.62	0.74	0.54	40.66
	M08-M08	1.66	0.56	0.76	0.74	37.30
	M09-M09	1.74	0.64	0.70	0.78	39.24
	M10-M07	1.81	0.63	0.69	0.83	43.39
	M10-M08	1.88	0.66	0.67	0.81	42.03
	M10-M05	1.96	0.52	0.78	0.82	39.29
	M10-M06	2.03	0.58	0.74	0.88	40.78
	M10-M09	2.16	0.64	0.69	1.00	39.77
	M10-M10	2.63	0.62	0.68	1.25	39.04